



Annual Report on Research Activities 2018 (Volume 8)



Tanabe Photonic Structure Group,
Department of Electronics and Electrical Engineering,
Faculty of Science and Technology, Keio University

Contents

Foreword	1
Lab Members	2
Research Activities	3
Dual-comb generation and soliton trapping in a single microresonator	4
Precise Dispersion Measurement for Ultra-high Q Microresonator	6
Fabrication of high-Q crystalline magnesium fluoride optical microresonators and experiments on dissipative Kerr soliton generation	8
PhC nanocavity integrated with p-i-n diode transmitter fabricated by photolithography fabrication process	10
Thermal vibration control using calcium fluoride microcrystal resonator	13
Fabrication of Er-doped Microresonator for On-chip Mode-locked Laser with CNT as Saturable Absorber	16
Theoretical analysis of mode-locking condition with Er + CNT	18
Stabilization of Brillouin laser in coupled silica toroid microcavities	20
Proposal and numerical study of non-reciprocal devices with magneto-optical effect	22
Statistical Data	25
Publications	26
Dissertations	28
Symposium	29

Foreword

Thank you very much for your continued support and interest in the research and educational activities at the Tanabe Photonic Nanostructure Laboratory, with the Department of Electronics and Electrical Engineering, in Keio University.

In this report, we will report on some of the research we conducted in FY2018. This year, we held an international symposium on microresonator frequency comb in Keio university. I am hoping that this gathering contributed to the growth of the microresonator frequency comb community in Japan and worldwide.

I would like to note that the manuscripts were written by my students with minimal editing; so if you have trouble with the language and contents, please do not hesitate to contact me. Although some of the papers might have some issue with the language, I would like to stress that I am confident that the research is of high impact and contains originality that will benefit the research community. If you are interested in our research, please contact us; we are always open for collaboration. Thank you very much for your interest.



December 2019
Takasumi Tanabe, Professor,
Department of Electronics and Electrical Engineering,
Keio University

Lab Members (Names and their positions after graduation)

Professor: Takasumi Tanabe

Secretary: Kaoru Onodera

PhD Students:

Nurul Ashikin Binti Daud

PhD in Engineering, Graduates the graduate school of Keio University

Ryo Suzuki

PhD in Engineering, Graduates the graduate school of Keio University

Shun Fujii

Continues in the graduate school of Keio University

Research Fellowship for Young Scientist, JSPS (DC1)

Master 2nd Grade: (The class of 2016)

Naotaka Kamioka

Graduates the graduate school of Keio University

Akihiro Kubota

Graduates the graduate school of Keio University

Motoi Kumasaki

Continues in the graduate school of Keio University

Mika Fuchida

Graduates the graduate school of Keio University

Yoshihiro Honda

Graduates the graduate school of Keio University

Tomoo Samuel Suzuki

Continues in the graduate school of Keio University(DD) (2018/9~)

Master 1st Grade: (The class of 2017)

Rammaru Ishida

Continues in the graduate school of Keio University

Shengi Jin

Continues in the graduate school of Keio University

Jocelyn Jack, Hoff

Continues in the graduate school of Keio University(DD) (2018/9~)

Bachelor 4th Grade: (The class of 2018)

Minoru Hasegawa

Graduate Keio University (2018/9)

Mizuki Ito

Graduate Keio University

Riku Imamura

Continues in the graduate school of Keio University

Nao Okuya

Graduate Keio University

Shuya Tanaka

Continues in the graduate school of Keio University

Koichiro Handa

Continues in the graduate school of Keio University

Research Activities

Dual-comb generation and soliton trapping in a single microresonator

Ryo Suzuki (D3)

Microresonator frequency combs (known as microcombs or Kerr combs) have a large repetition frequency ranging typically from 10 to 1000 GHz, which is compatible with fast-scanning applications including dual-comb spectroscopy and LiDAR. In this research, we numerically study dual-comb generation and soliton trapping in a single microresonator, whose two transverse modes are excited with orthogonally polarized dual pumping. The numerical simulation calculates the dual-comb formation in a microresonator, whose microcombs propagate as soliton pulses and cause soliton trapping depending on the parameters.

Key word: Microresonator, microcomb, dual-comb, soliton trapping

1. Introduction

Microresonator frequency combs, which are known as microcombs or Kerr combs, can provide attractive characteristics such as a low driving power due to their high quality factor (Q) and a small mode volume, compactness, and high repetition frequencies that correspond to the cavity-free spectral ranges (FSRs) [1]. The repetition frequency of microcombs is typically in the 10 to 1000 GHz range, which is higher than that of conventional optical pulse sources (<10 GHz) such as Ti:sapphire and fiber lasers. A microcomb is formed inside a microresonator via four-wave mixing (FWM) processes, which are excited with a continuous-wave laser by scanning the pump frequency from high to low.

The demonstration of a soliton (mode-locked) microcomb opened the way to many practical applications including optical communication with wavelength division multiplexing, microwave oscillators, optical frequency synthesizers, dual-comb spectroscopy, and LiDAR.

In dual-comb systems, which utilize two types of optical pulse trains with slightly different repetition frequencies, microcomb platforms can achieve fast scan rates for spectroscopy and LiDAR. This is because a dual-comb system with optical pulse trains at high repetition frequencies can allow a large difference between the repetition frequencies, which corresponds to the scan rate in measurement systems, with low noise. Hence the key parameter is the repetition frequency of each soliton microcomb in the time domain, which corresponds to the mode spacing between comb lines in the frequency domain.

There are certain approaches for generating a dual-comb in a microresonator system. One approach is to pump two different transverse modes (also known as mode families) in a single microresonator. In this system, both

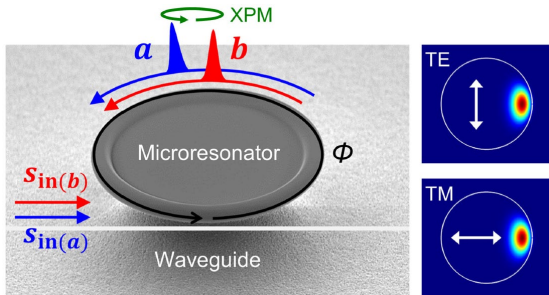


Fig. 1: Illustration of a simulation model with orthogonally polarized dual-pumping (left) and examples of mode intensity profiles in the TE and TM modes (right). Propagating solitons interact via XPM, which changes the group velocities.

combs share the same resonator (common mechanical vibrations and thermal fluctuations) and also the same feedback loops, which leads to mutual coherence between the combs.

When pumping two different transverse modes as illustrated in Fig. 1, control of the pump frequencies is typically required because two individual lasers are used to pump the resonance modes, which are located separately in the frequency domain. However, a large difference can be achieved between the repetition frequencies by controlling the pump frequencies and cavity dispersion of the pumped resonance modes. Also, cavity size and dispersion engineering can be used to control the resonance frequencies whose separation is at microwave levels (below tens of gigahertz). The different transverse modes can be pumped by using a single laser with an electro-optic modulation.

In this research, we theoretically study dual-comb generation in a single microresonator by using coupled Lugiato-Lefever equations (LLEs), and we focus particularly on soliton trapping. The conditions for dual-comb soliton generation and soliton trapping are investigated with numerical simulation and analysis approaches. [2]

2. Simulation model

Microcomb formation has been studied using an LLE [3]. To calculate multiple microcomb formation, two LLEs are coupled and developed by taking XPM and the difference between repetition frequencies into account. The time evolution of the internal fields a and b , which have orthogonal polarizations (TE and TM modes), are represented with coupled LLEs as

$$\frac{\partial a}{\partial t} = -\frac{\kappa_{(a)}}{2}a + i\Delta\omega_{0(a)}a + i\frac{D_{2(a)}}{2}\frac{\partial^2 a}{\partial\phi^2} + ig_{(a)}(|a|^2 + \sigma|b|^2)a + \sqrt{\kappa_{c(a)}}s_{in(a)} + \frac{\Delta D_1}{2}\frac{\partial a}{\partial\phi} \quad (1)$$

$$\frac{\partial b}{\partial t} = -\frac{\kappa_{(b)}}{2}b + i\Delta\omega_{0(b)}b + i\frac{D_{2(b)}}{2}\frac{\partial^2 b}{\partial\phi^2} + ig_{(b)}(|b|^2 + \sigma|a|^2)a + \sqrt{\kappa_{c(b)}}s_{in(b)} - \frac{\Delta D_1}{2}\frac{\partial b}{\partial\phi} \quad (2)$$

where t is a slow time and ϕ is the azimuthal angular coordinate inside the microresonator, which is related to the fast time. $\kappa_{(*)}$, $\kappa_{i(*)}$, and $\kappa_{c(*)}$ are the cavity decay, intrinsic decay, and coupling rates, respectively. They are related as follows $\kappa_{(*)} = \kappa_{i(*)} + \kappa_{c(*)}$. Here $(*)$ represents (a) or (b) . $\Delta\omega_{0(*)}$ is the detuning between the pump and resonance frequencies as $\Delta\omega_{0(*)} = \omega_{p(*)} -$

$\omega_{0(*)}$, where $\omega_{p(*)}$ and $\omega_{0(*)}$ are the pump and resonance frequencies, respectively. The resonance frequencies in one transverse mode follow a Taylor expanded equation as $\omega_{\mu(*)} = \omega_{0(*)} + D_{1(*)}\mu + D_{2(*)}\mu^2/2 + \dots$, where μ is the mode number offset from the pump mode, $D_{1(*)}$ is the cavity FSR, and $D_{2(*)}$ is the second-order dispersion. $g_{(*)}$ is a nonlinear coefficient $g_{(*)} = (\hbar\omega_0^2 n_2 D_{1(*)}) / (2\pi n^2 A_{\text{eff}(*)})$, where \hbar is the reduced Planck constant, n_2 is the nonlinear refractive index, n is the refractive index, and $A_{\text{eff}(*)}$ is the effective mode area. σ is the XPM coefficient ($\sigma = 2/3$ for orthogonal polarizations), $s_{\text{in}(*)}$ is the input field as $s_{\text{in}(*)} = \sqrt{P_{(*)}/\hbar\omega_{0(*)}}$, $P_{(*)}$ is the input power, and ΔD_1 is the difference between the cavity FSRs of two transverse modes where $\Delta D_1 = D_{1(b)} - D_{1(a)}$.

Here, we calculate generalized coupled LLEs:

$$\frac{\partial u}{\partial \tau} = -(1 + i\alpha_{(u)})u + i\beta_{(u)}\frac{\partial^2 u}{\partial \phi^2} + i(|u|^2 + \sigma|v|^2)u + F_{(u)} + \gamma\frac{\partial u}{\partial \phi} \quad (3)$$

$$\frac{\partial v}{\partial \tau} = -(1 + i\alpha_{(v)})v + i\beta_{(v)}\frac{\partial^2 v}{\partial \phi^2} + i(|v|^2 + \sigma|u|^2)v + F_{(v)} - \gamma\frac{\partial v}{\partial \phi} \quad (4)$$

where we assume $\kappa = \kappa_{(a)} = \kappa_{(b)}$ and $g = g_{(a)} = g_{(b)}$. The parameters follow $\tau = kt/2$, $u = a\sqrt{2g/\kappa}$, $v = b\sqrt{2g/\kappa}$, $\alpha_{(**)} = -2\Delta\omega_{0(*)}/\kappa$, $\beta_{(**)} = D_{2(*)}/\kappa$, $\gamma = \Delta D_1/\kappa$, and $F_{(**)} = (2s_{\text{in}(**)}/\kappa)\sqrt{2g\kappa_{c(*)}/\kappa}$, where $\{(*)$, $\{(**)\}$ represents $\{(a), (u)\}$ or $\{(b), (v)\}$. Here, when the parameters are set at $\sigma = 0$ and $\Delta D_1 = 0$, Eqs. (1)-(4) are regarded as a basic LLE, which does not take account of the interaction between each equation.

3. Numerical simulation results

Figure 2 shows the time evolution of microcomb spectra and waveforms for two orthogonally polarized transverse modes when the α value is changed from negative to positive. The simulation was performed using a split-step Fourier method with a MATLAB code. There are 1023 calculated modes in each transverse mode. The parameters are $\alpha = \alpha_{(u)} = \alpha_{(v)}$, $\beta_{(u)} = \beta_{(v)} = 0.01$, $\gamma = 0.3$, and $F_{(u)} = F_{(v)} = 4$. Since γ is a nonzero value, two solitons in each transverse mode propagate at different group velocities, which is shown at a τ of around 70-100 in Fig. 2(b). However, XPM compensates for the group velocity mismatch over a τ of 100 shown by the white arrow regions, where the two solitons propagate at the same group velocity and they remain at the same position inside a microresonator.

At the top of Fig. 2(b), an XPM induced trapped soliton is directly generated from the original soliton of an internal field u . On the other hand, at the bottom of Fig. 2(b), the trapped soliton is not directly generated from the original soliton of an internal field v (which is represented around a τ of 90). In our simulation, a trapped soliton is seeded by one of the original solitons in two transverse modes.

Figure 3 shows the comb spectra and waveforms at a τ of 120 seen in Fig. 2. The XPM compensates mutually for the group velocities that cause the center frequencies of the

comb envelopes to shift in opposite directions as shown in Fig. 3(a). The shift $\Delta\mu$ follows $\Delta\mu = \Delta\omega_c/D_1 = \pm\Delta D_1/(2D_2)$ for fields a (u) and b (v), respectively. Here $\Delta\omega_c$ is the amount of center frequency shift in units of rad/Hz. This theoretical value is in good agreement with our numerical simulation results. Although Fig. 3 shows the formation of a single trapped soliton, the soliton number is random as in the LLE simulation.

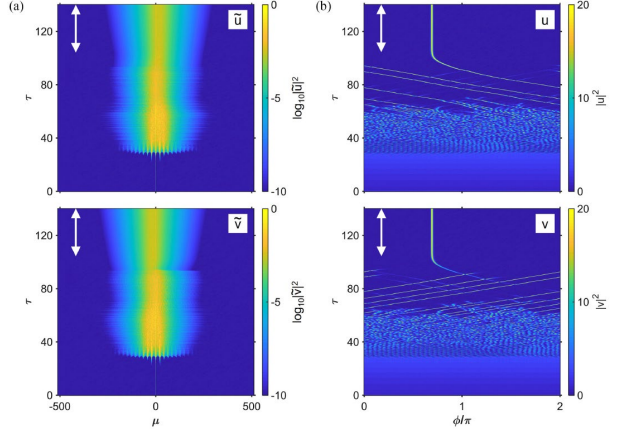


Fig. 2: Time evolution of microcomb (a) spectra and (b) waveforms in each transverse mode while changing α from a negative to a positive value. White arrows represent soliton trapping regions where two solitons are coupled via XPM and propagate at the same group velocity.

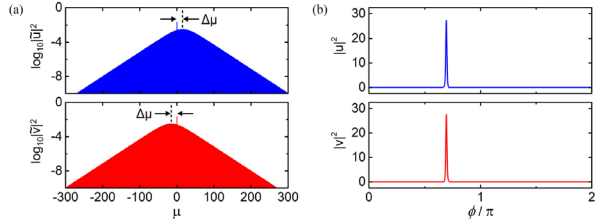


Fig. 3: Trapped soliton microcomb (a) spectra and (b) waveforms in each transverse mode at a τ of 120 in Fig. 2. Soliton trapping is induced by XPM, which shifts the center frequencies of the comb envelopes and keeps the solitons at the same position inside the microresonator.

4. Summary

We numerically and theoretically studied dual-comb generation and soliton trapping in a single microresonator, whose two transverse modes were excited with orthogonally polarized dual-pumping (TE and TM modes). The simulation model employed coupled LLEs, which take account of the XPM and the difference between repetition frequencies. The numerical simulation calculated the dual-comb formation in a microresonator, whose microcombs propagated as soliton pulses and caused soliton trapping depending on the parameters [2].

References

- [1] T. J. Kippenberg, *et al.*, *Science* **361**, eaan8083 (2018).
- [2] R. Suzuki, *et al.*, *IEEE Photon. J.* **11**, 6100511 (2019).
- [3] Y. K. Chembo, *Nanophotonics* **5**, 214–230 (2016).

Precise Dispersion Measurement for Ultra-high Q Microresonator

Shuya TANAKA (B4)

Optical frequency combs generated in optical microresonators (microcombs or Kerr combs) exhibit an extremely high repetition frequency reaching GHz-THz as an ultrashort pulse light source and have the potential for a wide range of applications. A whispering gallery mode (WGM) microresonator fabricated from magnesium fluoride (MgF₂) crystals can efficiently generate microcombs, as it achieves both a very high Q factor of up to 10⁸ and a small mode volume. However, resonator dispersion has a strong influence on microcomb generation. Therefore, if dispersion can be controlled and measured precisely, it will bring about a further breakthrough in microcomb generation. In this study, for an ultra-high Q MgF₂ resonator designed and manufactured by ultra-precision machining adjustable to nm order, we measured its dispersion precisely using different methods and compared each method. As a result, significant differences were observed between each method, and it was confirmed that they were in good agreement with the theoretical calculation.

Key words: microresonator, microcomb, dispersion measurement, ultra-precise machining

1. Introduction

In recent years, progress has been made on the development of optical frequency combs based on microresonators (microcombs), where such combs are often operating in the dissipative soliton regime (dissipative Kerr soliton; DKS) as a result of mode-locking with the comb components. And optical frequency combs have been widely accepted as ultrafast pulsed light sources [1]. Their repetition frequency coincides with the free spectral range (FSR) of the resonator and reaches an extremely high region of GHz to THz. The difference is clear when compared with that of 10 GHz or less obtained with existing pulsed lasers such as Ti:sapphire lasers and fiber lasers. On the other hand, because of the high Q factor and small mode volume of the resonator, it also has the advantage that low power driving and miniaturization are possible [1].

In WGM microresonators, the m -th resonance mode frequency is expressed as follows;

$$\omega_m = \frac{2\pi c}{L \cdot n(\omega)} m, \quad (1)$$

where, c is the speed of light, and L is the waveguide length of the resonator. When the internal power exceeds the threshold, cascaded four-wave mixing (FWM) occurs, and microcombs will be generated. Due to the dispersion $n(\omega)$ of the resonator, the actual FSR gradually changes, which affects the frequency broadening of the microcomb. Basically, an anomalous dispersion is required because the resonance frequency shifts due to anomalous dispersion and the optical Kerr effect cancel each other out. This balancing assists the frequency spanning of microcombs and DKS formation. Therefore, a consideration of resonator dispersion is an essential technological element for microcomb generation.

The effect of dispersion is expressed by the following Taylor expansion, where the μ -th resonance mode frequency is counted relative to the resonance mode centered on the pump light;

$$\omega_\mu = \omega_0 + D_1\mu + \frac{1}{2}D_2\mu^2 + \dots, \quad (2)$$

where, ω_0 corresponds to the frequency of the pump mode, D_1 corresponds to the resonator FSR when there is no dispersion. Coefficients after D_2 indicate the influence

of dispersion. In most cases, third-order or higher terms can be ignored.

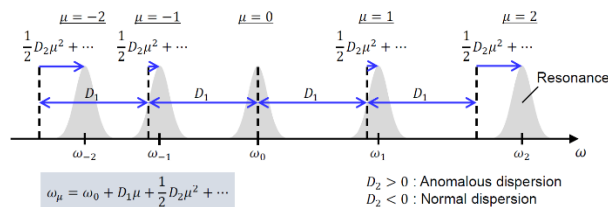


Fig. 1: Resonance modes considering resonator dispersion.

Eq. (1) and (2) hold only in a specific transverse mode. Since microresonators are multimode waveguides, different transverse modes can interact and generate mode coupling. Hence, the resonance mode that should originally generate one of the comb lines is affected, and microcomb generation is inhibited. Information about such mode coupling can also be obtained by dispersion measurement, so precise measurement is also required.

In this research, several dispersion measurement methods were simultaneously implemented, and each obtained measurement result was examined in terms of measurement accuracy.

2. Dispersion measurement methods

For dispersion measurement, it is sufficient to obtain the transmission spectrum over a wide range and find the peak intervals. There are two important points: securing the number of samples for one resonance spectrum, and the peak interval measurement accuracy. In general, based on Eq. (2), the trend of the peak interval (FSR) is fitted by a quadratic function to obtain the dispersion D_2 .

In the resonator, the linewidth of its resonance spectrum becomes narrower as its Q factor increases, so it is necessary to sample around the peak with high resolution. This is the key to the first point, and it is handled by a high-performance oscilloscope (OSC).

Since the data acquired by the OSC is on the time axis, it has to be converted to the frequency axis to obtain a transmission spectrum. Therefore, together with the transmission waveform of the resonator, it is necessary to simultaneously measure any data that carry the frequency "marker". The frequency stability of this marker is the

measurement accuracy. Here, measurement methods are classified into three types according to the system to be used as a marker. That is, 1. a wavemeter, 2. a Mach-Zehnder interferometer (MZI) [2], and 3. fiber laser-based mode-locked optical frequency combs (fiber combs) [3]. In method 1, the wavelength axis is configured directly for reading the wavelength-swept during transmission spectrum acquisition with a wavemeter built into the laser. This is the easiest and quickest measurement. In particular, if the transmitted power is also acquired simultaneously with DAQs, all processing can be performed by computers. However, the built-in wavemeter has poor measurement accuracy, and DAQs tend to result in insufficient resolution due to the lack of an OSC. In method 2, a sinusoidal wave is acquired by interference and its period is used as the scale of the frequency axis. An MZI can be easily made from fiber alone, and the interference fringe period (= frequency scale) is adjustable simply by changing the delay length. However, since the interference wave period is subject to the dispersion of the fiber, the fiber dispersion must be separately measured and calibrated [2]. Method 3 uses a fiber comb that boasts outstanding frequency stability, so the measurement accuracy is extremely high. On the other hand, the measurement system becomes very complicated because the marker is generated by mixing with the pump laser, not directly using the fiber comb [3].

3. Measurement results and comparison

The measured resonator is shown in Fig. 2. Parameters such as diameter or cross-sectional shape were designed and realized by ultra-precision machining. The Q factor was approximately 1.7×10^8 , which is sufficiently high.

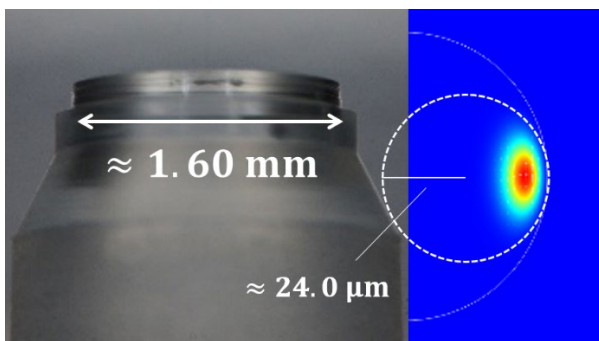


Fig. 2: The MgF_2 microresonator used in this research. The diameter, cross-sectional shape, and size of the WGM waveguide can be designed because ultra-precision machining is used.

For this resonator, we can theoretically calculate the dispersion. We performed all the above methods (1. wavemeter (with DAQ or OSC), 2. MZI (also considering calibration), and 3. fiber comb) simultaneously with this resonator and measured the dispersions and compared them with the theoretical dispersion curves. A summary of the obtained measurement results is provided in Fig. 3. This resonator has anomalous dispersion because both measured and theoretical values are downward convex quadratic curves. In addition, mode coupling was observed around $\mu = 100, 150$ in common with all the measurement results. Compared with the DAQ result, there were new plots in the result obtained using the wavemeter with the

OSC. This means that the resolution has been improved by the OSC with the measurement accuracy unchanged. In the MZI method, the variation improved significantly. Although, after calibration, the result agrees very well with the theoretical curve, it can be seen that calibration is essential because without it the curve is distorted and becomes upwardly convex. With the fibercomb method, this result was obtained directly, so the reliability of the frequency marker was very high as expected. In the results obtained with the MZI and fibercomb method, the difference in the variance is the same because the resolution of the OSC reached the limit, and there remains room for improvement. From the above, it is sufficient to use a wavemeter if we look only at the tendency of the coarse dispersion, but in situations where precision is required such as microcomb generation, measurement methods that use calibrated MZIs or fibercombs are more suitable.

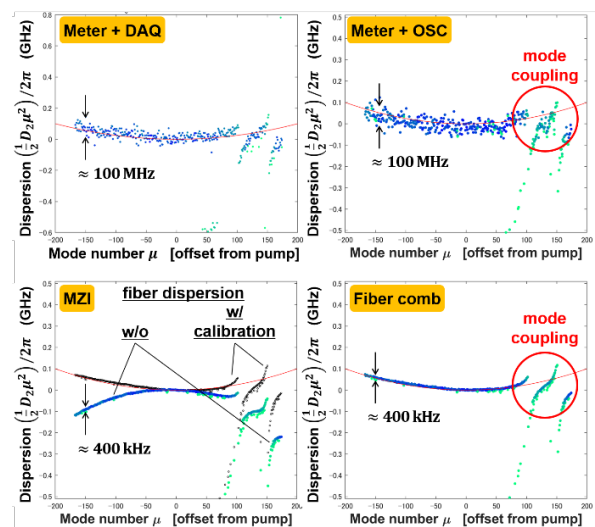


Fig. 3: Dispersion measurement results obtained with each method. Each point corresponds to the resonance spectrum of the mode family of interest, and the closer it is to the blue plot, the stronger the resonance becomes. The values indicated by arrows represent the scatter range of the measured values.

4. Conclusion

In this study, the dispersion was measured with different methods using frequency markers for ultra-high Q MgF_2 crystalline microresonators controlled and fabricated by precise machining. As a result, the difference between the measurement results due to marker accuracy, and good agreement with the theoretical value that can be calculated by distributed control were confirmed. In other words, we have successfully established dispersion measurement technology. In the future, by further promoting the combination of this result and the design and control of dispersion with ultra-precision machining, we can optimize the fabrication of microresonators for the generation of flexible microcombs and solitons.

References

- [1] T. J. Kippenberg, *et al.*, *Science* **361**, eaan8083 (2018).
- [2] Xu Yi, Ph. D thesis, Caltech (2017).
- [3] P. Del'Haye, *et al.*, *Nat. Phot.* **3**, 529-533 (2009).

Fabrication of high-Q crystalline magnesium fluoride optical microresonators and experiments on dissipative Kerr soliton generation

Akihiro Kubota(M2)

The crystalline magnesium fluoride microresonator is a whispering gallery mode (WGM) resonator. WGM microresonators have a very high quality factor, which means they can confine light to a small volume for long periods of time. Recently, a new method of optical frequency comb generation using a microresonator, which is called a Kerr comb, has attracted a lot of attention. In this research, we fabricated a crystalline magnesium fluoride microresonator and measured the quality factor. With the microresonator, we conducted an experiment aimed at Kerr comb generation and dissipative Kerr soliton formation.

Key words : Optical microresonator, Kerr frequency comb, dissipative Kerr soliton

1. Background

An optical frequency comb is an optical signal with many frequency components with an equal line spacing [1]. An optical frequency comb is, for example, generated by using a mode-locked laser such as a Ti:sapphire laser or a fiber laser. A technique for precise frequency measurement with an optical frequency comb was established by T. W. Hänsch of the Max Planck Institute of Quantum Optics (MPQ) and J. L. Hall of the Joint Institute for Laboratory Astrophysics (JILA). In 2005, they won the Nobel Prize in Physics for their contribution to developing precise metrology with a frequency comb.

Recently, optical frequency combs from a microcavity have been researched with more interest. Such an optical frequency comb is called a Kerr comb. A Kerr comb is generated with a WGM microcavity, which has a high-quality factor and can confine light to a small volume for long periods of time. In the microcavity, the interaction between light and matter is enhanced, and so various optical nonlinear effects can be generated efficiently. A Kerr comb is an optical frequency comb generated via cascaded four-wave mixing in a microcavity. The Kerr comb has the potential for miniaturization, cost reduction, and energy-saving [2,3].

The quality factor of a crystalline magnesium fluoride microresonator is higher than that of a silica microresonator and a silicon nitride microresonator. This is because magnesium fluoride absorbs less light. Many applications have already been proposed including large-capacity optical communication [4], and microwave generation [5].

2. Fabrication of crystalline magnesium fluoride microresonator

A crystalline magnesium fluoride microresonator is fabricated by using a cutting and polishing process with an air spindle. The procedure is as follows. First, the crystalline magnesium fluoride material is fixed to a brass rod. Then, the material is cut with a diamond cutter and sandpaper. After the cutting process, the material is polished with diamond paste. Fig. 1 shows the variation in the crystalline magnesium fluoride material after each process.

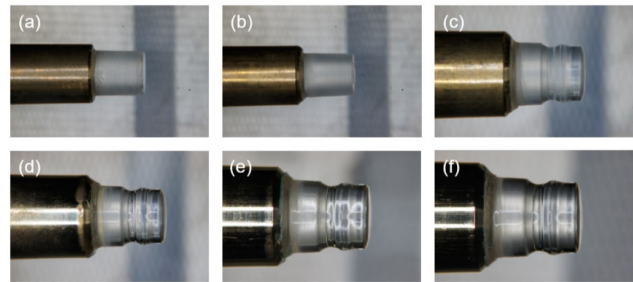


Fig. 1 : Change in the crystalline magnesium fluoride material after each process. (a) The crystalline magnesium fluoride material before the machining process. The material is fixed to the brass rod. (b) The surface of the material is cut to correct the axial runout. (c) The microresonator shape is formed. (d - f) After the polishing process. Polishing pastes including different sized diamond particles are used at (d-f). The particle sizes are as follows. (d) 3 μm , (e) 1 μm , (f) 0.05 μm .

3. Characterization of crystalline magnesium fluoride microresonator

We conducted characterization experiments on the fabricated crystalline magnesium fluoride microresonator. The quality factor of the microresonator was measured with the ringdown method. We used tapered fiber for optical coupling into the microresonator. Fig. 2 shows an image of the fabricated crystalline magnesium fluoride microresonator. The microresonator is 3.95 mm in diameter and the free spectral range (FSR) = 17.6 GHz. Fig. 3 shows the result of the ringdown measurement. The quality factor is 3.7×10^9 .

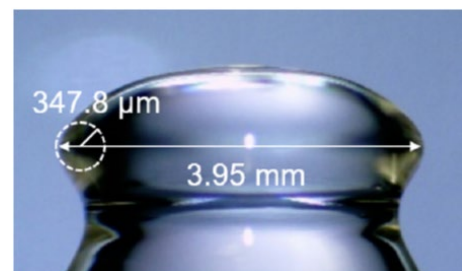


Fig. 2 : Crystalline magnesium fluoride microresonator. The diameter is 3.95 mm and the FSR = 17.6 GHz.

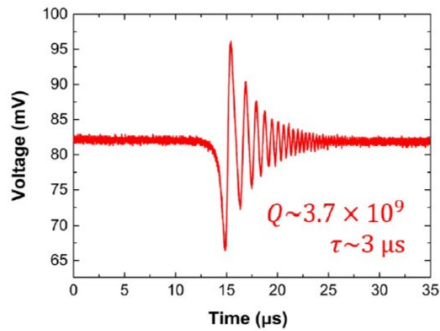


Fig. 3 : Result of ringdown measurement.

4. Experiments on Kerr comb generation & dissipative Kerr soliton generation

We conducted experiments on Kerr comb generation and dissipative Kerr soliton generation with the fabricated crystalline magnesium fluoride microresonator. In the experiment, a Kerr comb was generated by sweeping the pump laser frequency from the blue side to the red side of the resonant frequency of the microresonator. Fig. 4 shows the Kerr comb spectrum, which was generated by cascaded four-wave mixing in the crystalline magnesium fluoride microresonator. We used a microresonator with a diameter of 3.95 mm (FSR = 17.6 GHz) in the experiment.

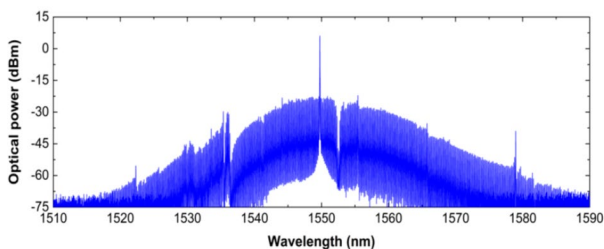


Fig. 4 : Kerr comb spectrum obtained by using a crystalline magnesium fluoride microresonator with a diameter of 3.95 mm. A single-frequency CW fiber laser was used as an external pump laser whose linewidth was 0.1 kHz.

Mode-locked Kerr frequency comb generation has recently been reported [6], and related applied research is attracting a lot of attention. In this research, we conducted experiments on mode-locked Kerr comb generation. When the Kerr frequency comb is mode-locked, an optical soliton is present in the microresonator in the time domain. The optical soliton in the microresonator is called a dissipative Kerr soliton. When the pump laser frequency is swept in the experiment and the dissipative Kerr soliton is generated, the transmittance of the output light from the microresonator changes stepwise. The step-like signals are called soliton steps and they indicate the existence of a dissipative Kerr soliton. Fig. 5 shows the soliton step signal that is obtained by using the fabricated crystalline magnesium fluoride microresonator. In the experiment, we used a tunable laser source with a linewidth of 100 kHz.

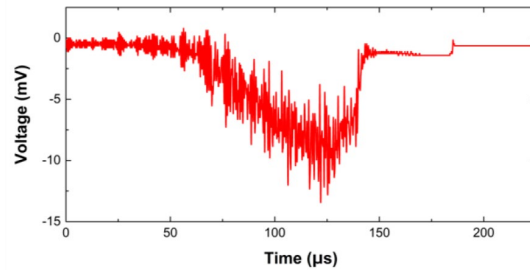


Fig. 5 : Soliton step signal obtained by using a crystalline magnesium fluoride microresonator with a diameter of 3.95 mm.

We obtained a soliton step signal with the fabricated microresonator and the laser has wide tunability. However, we could not obtain a mode-locked Kerr comb spectrum. Fig. 6 shows the beat note signal of the Kerr comb in Fig. 4. This beat note signal corresponds to the repetition frequency of the Kerr comb. The beat note signal of the mode-locked Kerr frequency comb has only one peak, and the linewidth is less than 1 kHz. The beat note signal in Fig. 6 has two peaks and the linewidth exceeds 1 MHz. This means that the Kerr comb in Fig. 4 is not mode-locked.

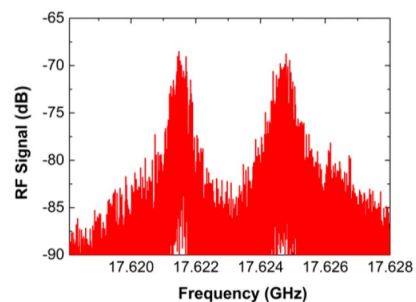


Fig. 6 : Beat note signal of the Kerr comb in Fig. 4.

4. Conclusion

We fabricated a crystalline magnesium fluoride microresonator. We conducted experiments to characterize the fabricated microresonator. The quality factor was 3.7×10^9 . With the microresonator, we conducted experiments on Kerr comb generation and dissipative Kerr soliton generation. A soliton step signal was obtained.

Reference

- [1] 洪鋒雷, 応用物理学会 **36**(2), 60-67 (2007).
- [2] P. Del'Haye, et al., Phys. Rev. Lett. **107**, 063901 (2011).
- [3] T. J. Kippenberg, et al., Science **332**, 555-559 (2011).
- [4] J. Pfeifle, et al., Nat. Photon. **8**(5), 375-380 (2014).
- [5] L. Maleki, Nat. Photon. **5**(12), 728 (2011).
- [6] T. Herr, et al., Nature Photonics **8**, 145-152 (2014).

PhC nanocavity integrated with p-i-n diode transmitter fabricated by photolithography fabrication process

Nurul Ashikin Binti Daud (D3)

Passive and active optical devices with a high-Q SiO₂-clad PhC nanocavity, such as an electro-optic a modulator, a photodetector, and a demultiplexer filter, have been demonstrated. This study describes an all-Si scheme PhC nanocavity integrated with p-i-n diode transmitter. Light modulation can be transmitted and detected by the PhC nanocavity structure. A 100 MHz square pulse and a 2⁵-1 PRBS NRZ signal were demonstrated in a back-to-back transmission operation.

Key words: Photonic crystal; Silicon photonics; Optical switching; Integrated optics

1. Introduction

Over 30 years ago, Gordon Moore's prediction that the number of transistors per integrated circuit would double every two years has become a reality [1]. This has driven a dramatic scaling in feature sizes especially as regards short distance communication. Furthermore, the limitations of electrical signals over copper cables have also started to become apparent. This is because the resistance in copper wire distorts the signal [2].

Silicon photonics is regarded as a technology with the potential to solve this problem because photons do not produce Joule heating. So, a silicon photonics approach will not affect data transmission. Moreover, the high refractive index and low absorption loss of silicon at telecom wavelengths make it possible to realize low-loss waveguides on a chip thanks to the use of sophisticated fabrication technologies.

The mature CMOS manufacturing techniques that are now available have been widely used in the telecommunication industry. Currently, most optical devices are CMOS compatible. This will allow easier integration with other silicon photonics devices on a single chip.

The strong light confinement provided by a 2D PhC has allowed us to demonstrate various optical devices based on a high-Q PhC nanocavity [3]–[5]. Of these devices, electro-optic (EO) and opto-electronic (OE) devices are key components when linking electrical circuits with photonics circuits. Nowadays, the aim of most researchers is to achieve devices that are compact, easy to fabricate and cost-effective. In particular, the key interfaces bridging the EO and OE devices on the same chip are crucial for a fully functional optical interconnect system.

However, the transparency of silicon at telecom wavelengths meant that photo-carriers could not be generated. Commercial silicon photonics transceivers currently use silicon modulators together with epitaxially grown germanium on silicon or heterogeneously bonded III-V

photodetectors [6], [7]. Although at present these methods are effective, they will be inadequate for use with the fast developing optical chip-level integration, which requires a compact size, a low fabrication cost and simple packaging.

Therefore, researchers have started to consider all-silicon transceiver devices. A similar study was previously reported that utilized a Mach-Zehnder interferometer (MZI) structure. However, the leak current at -3 V is relatively large at 4.1 nA, and the large footprint of the device is a disadvantage. In this study, we demonstrate a CMOS compatible PhC nanocavity transceiver for power monitoring.

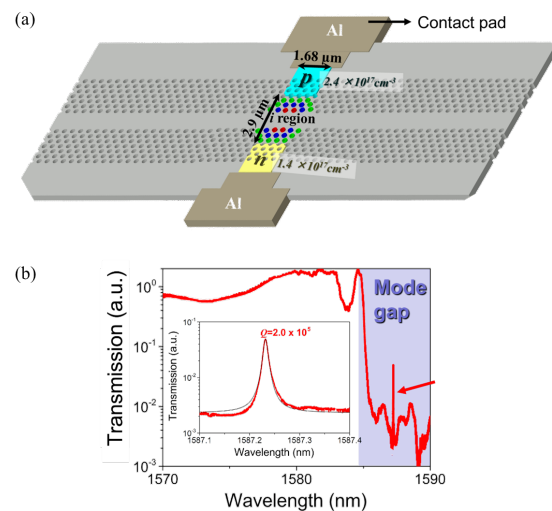


Fig. 1: (a) Schematic illustration of a PhC nanocavity with a p-i-n junction. (b) Transmittance spectrum of the structure.

2. Device structure

Fig. 1(a) shows the design of our photonic crystal nanocavity device. The cavity is fabricated in the *i* region, which is between the *p* and *n* regions. The doping densities for the *p* and *n* regions are 2.4×10^{17} and 1.4×10^{17} cm⁻³, respectively. The width and the distance between the *p* and *n* regions are both 2.9 μ m. We measured the transmission spectrum of this PhC nanocavity and obtained a very high loaded *Q* of 2.0×10^5 at a wavelength of

1587.35 nm, as shown in Fig. 1 (b). A high Q is achieved by employing photolithographic fabrication. We have reported a similar demonstration elsewhere, but now we have integrated the device with a *p-i-n* junction.

3. Measurement method

To conduct the PhC transmitter demonstration, two PhC structures are required for a signal modulator (Tx) and a signal receiver (Rx). Thus, it is essential to pre-select a pair with the two highest Q values and with a similar resonance wavelength. We chose a PhC nanocavity structure for the Tx and a PhC waveguide structure for the Rx for the transmitter demonstration. Both resonance wavelength structures are shown in Fig. 2 (a). As shown in the figure, there is an approximately ~ 1 nm resonance wavelength difference between the two PhC structures. Therefore, temperature-dependent operation is essential if we are to control the position of the resonance wavelength. Fig. 2 (b) shows the temperature-dependent operation system. Fig. 2 (c) shows the resonance shift of the Tx resonance wavelength when heat is applied to the structure. The resonance wavelength of the Tx shifted ~ 1 nm from that at room temperature when the sample was heated to 39 °C. Note that there will be a large fluctuation if the temperature is set at a high temperature (e.g. 50 °C) due to the thermal expansion of the sample and the system. Thus, it is important to find the closest resonance wavelength.

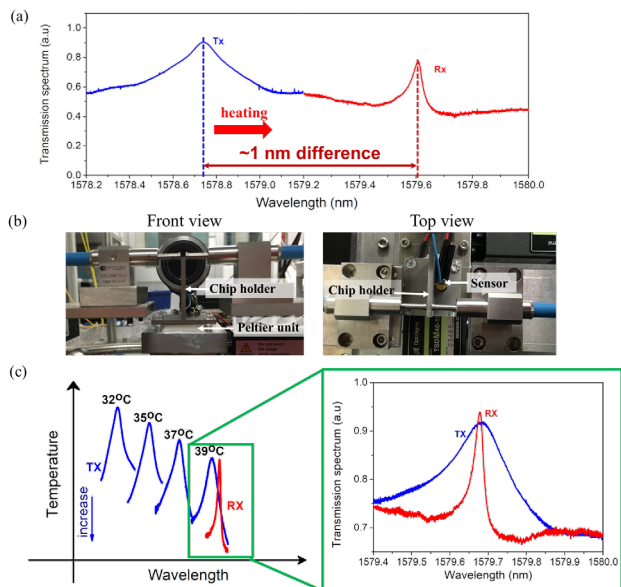


Fig. 2: (a) Difference between Tx and Rx resonance wavelengths. (b) Temperature-dependent operation system. (c) Tx resonance shift after heating.

Next, we demonstrated the transmitter operation. The measurement setup is illustrated in Fig. 3 (a), which shows a back-to-back measurement. The wavelength was set at 1579.70

nm for the Tx component. A square pulse with a 100 MHz repetition rate was transmitted from the pulse-pattern generator to the Tx component. The power is boosted by the EDFA and the noise is eliminated by the band-pass filter. Then, the filtered optical signal is coupled to the Rx component. A reverse-biased voltage of -3 V is applied to the Rx component, and finally the output electric signal is amplified by a trans-impedance amplifier (TIA) with gain of 5×10^3 V/A.

The power of the modulated optical signal after the PhC nanocavity modulator was monitored before the EDFA where the value was 1.99 μ W. The optical signal was amplified to 0.63 mW after passing through the EDFA and BPF before reaching the Rx. Next, a 2^5 -1 pseudo-random bit sequence signal (PRBS) at 0.1 GHz was transmitted and observed at the oscilloscope as shown in Fig. 3 (d).

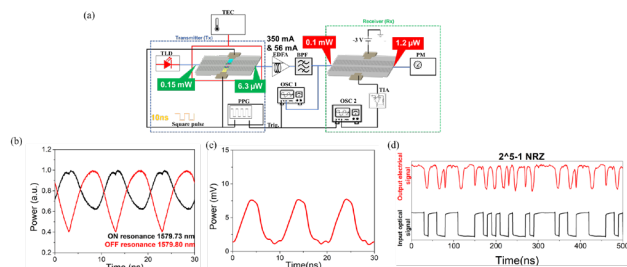


Fig. 3: (a) Transmitter operation system demonstration. (b) Output signal monitored at OSC1. (c) Output signal monitored at OSC2. (d) PRBS of 2^5 -1-bit sequence at 0.1 GHz.

Fig.4(a) shows the measurement setup for a 5 m transmission link and the signals observed at the Tx and Rx. A 50 MHz square pulse signal and an NRZ 2^5 -1-bit sequence PRBS signal were transmitted as shown in Fig. 4 (d).

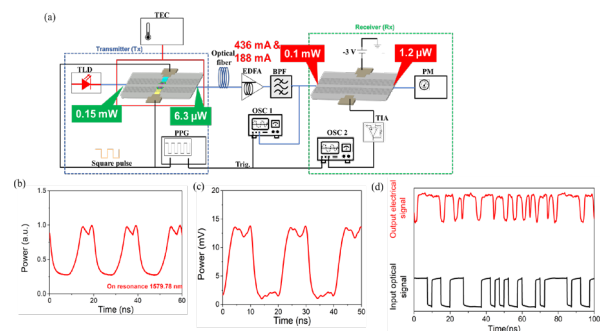


Fig. 3: (a) Transmitter operation system demonstration of 5 m transmission link. (b) Output signal monitored at OSC1. (c) Output signal monitored at OSC2. (d) PRBS of 2^5 -1-bit sequence at 0.05 GHz.

4. Discussion

The results show that the maximum operating speed of the device is 100 MHz in a back-to-back

operation. The obtained preliminary results indicate that the proposed device structure has the potential to be practically integrated as an optical transmission link system. However, this will be realized only after further improvement of the operating bandwidth, which can be achieved by optimizing the doping concentration and fabricating a small Al contact pad. By overcoming the limiting factor of the device, the expected bandwidth could be increased to \sim GHz.

Since the operating speed of the device is very low, it is very important to fully optimize the device. Therefore, despite it usually being essential to measure the optical transmission link system bit-error rate (BER) to determine the quality of a transmission system, it could not be accomplished at this stage. However, BER measurement will be essential with an optimized PhC nanocavity device.

Both PhC nanocavity devices used in this study were fabricated using a photolithographic fabrication technique. They are compatible with CMOS devices, and the presence of SiO₂ cladding makes the device robust and stable. Although photolithographic fabrication is not as precise as EB lithography, and fabrication error is expected, the study has shown that despite fabrication errors caused by random factors, we realized a functional optical device. On the other hand, thanks to the simple fabrication method and dense integration of the all-silicon scheme, we can expect large-scale production at reduced cost, which constitutes an option for constructing future transmission links.

A recent study has shown that the silicon photonic optical transmission link device is now being developed for chip-to-chip and on-chip transmission link systems [8]. Therefore, despite optimization, as future work, it will be necessary to integrate both chips (Tx and Rx) monolithically (on a single chip). Integration on a single chip is possible since we fabricated the device using a mature silicon foundry fabrication process.

5. Summary

An all-Si transmitter and receiver scheme with a CMOS compatible PhC structure was described. The system utilized both a PhC nanocavity structure and a PhC-WG random structure that constitutes a PhC structure capable of being utilized even in the presence of fabrication error. The 5 m transmission of a 0.05 GHzs⁻¹ 2⁵-1-bit NRZ signal was successfully modulated and detected in the system. This is the first demonstration of a transmitter and receiver with a PhC structure, and it shows that the device has the potential for use as an all-Si transmission link in the near future.

References

- [1] M. Lundstrom, "Moore's Law forever?," *Science (80-)*, vol. 299, no. 5604, pp. 210–212, 2003.
- [2] N. Savage, "Linking with light," *IEEE Spectr.*, vol. 39, no. 8, pp. 32–36, 2002.
- [3] N. A. B. Daud, Y. Ooka, T. Tabata, T. Tetsumoto, and T. Tanabe, "Electro-optic modulator based on photolithography fabricated p-i-n integrated photonic crystal nanocavity," *IEICE Trans. Electron.*, vol. E-100-C, no. 8, pp. 670–674, 2017.
- [4] N. A. B. Daud and T. Tanabe, "Photolithographically fabricated silicon photonic crystal nanocavity photoreceiver with laterally integrated p-i-n diode," *AIP Adv.*, vol. 8, no. 105224, 2018.
- [5] Y. Ooka, T. Tetsumoto, N. A. B. Daud, and T. Tanabe, "Ultrasmall in-plane photonic crystal demultiplexers fabricated with photolithography," *Opt. Express*, vol. 25, no. 2, pp. 1521–1528, 2017.
- [6] T. Pinguet *et al.*, "Monolithically integrated high-speed CMOS photonic transceivers," in *2008 5th IEEE International Conference on Group IV Photonics*, 2008, vol. 1, pp. 362–364.
- [7] L. Chen, K. Preston, S. Manipatruni, and M. Lipson, "Integrated GHz silicon photonic interconnect with micrometer-scale modulators and detectors," *Opt. Express*, vol. 17, no. 17, pp. 15248–15256, 2009.
- [8] A. H. Atabaki *et al.*, "Integrating photonics with silicon nanoelectronics for the next generation of systems on a chip," *Nature*, vol. 556, no. 7701, pp. 349–354, 2018.

Thermal vibration control using calcium fluoride microcrystal resonator

Koichiro Handa (B4) Ryo Suzuki (D3) Mika Fuchida (M2) Shun Fujii (D1)

A whispering gallery mode (WGM) resonator has a very small mode volume and a very high light confinement performance. A WGM microresonator can realize a large internal power simply when we input a low-power laser light from the outside. Therefore, it is suitable for microcomb generation using a non-linear effect. However, as the temperature changes, the resonant wavelength of light in the microresonator fluctuates due to the heat. In this study, using a crystalline calcium fluoride microresonator, we propose a method for suppressing thermal expansion by employing a metal heat sink on the resonator axis, and evaluate its characteristics.

Key words: Optical microresonator, Kerr effect, Thermo-opto-mechanical oscillation

1. Introduction

Various approaches have been studied for the efficient generation of nonlinear optical effects using the high Q values of microresonators and their large internal powers. In particular, microcomb generation has been studied in recent years [1]. A microcomb is light with a comb-like spectrum output from a micro-optical resonator, which uses four-wave mixing (FWM) that occurs inside the resonator when light from an external CW laser is input into the resonator. Furthermore, a soliton microcomb in which the phases of the microcombs are aligned in a micro-optical resonator has many applications including frequency calibration for wavelength-multiplexed optical communication with wavelength division multiplexing, a dual comb and LiDAR [1].

Since a strong light intensity can be obtained inside a micro-optical resonator, the temperature of the entire structure and the mode portion of the resonator increases due to such factors as material absorption. In this case, there is a shift in the resonant wavelength because the length of the structure changes due to thermal expansion, and the refractive index of the material changes due to the thermo-optic effect [2].

Calcium fluoride microcrystal resonators have many advantages such as the provision of a high quality factor (Q) with polishing [3] and low material absorption characteristics in a long wavelength region [4]. However, the thermal expansion coefficient and the thermo-optic coefficient have positive and negative values, respectively, and thermal expansion responds slowly to changes in the internal power of the resonator compared with the thermo-optic effect, and so the two effects do not occur simultaneously. As a result, when light propagates through a resonator, the resonance frequency oscillates due to heat (thermo-opto-mechanical (TOM) oscillation).

In this study, we propose a method for suppressing the thermal expansion by placing a metal heat sink on the central axis of the calcium fluoride resonator. We measured the change in the

thermal vibration with and without the heat sink and calculated the TOM oscillation.

2. Proposal for suppressing TOM oscillation of calcium fluoride microresonator

A conventional calcium fluoride resonator cannot be applied to an object with a stable frequency such as an optical Kerr comb due to TOM oscillation. In this study, we propose a hybrid resonator, which is a calcium fluoride crystalline resonator with a metal heat sink on its central axis. The hybrid resonator has brass, which has high thermal conductivity, inserted in it as a heat sink, and heat is expected to be efficiently diffused. Fig. 1 shows an outline of the hybrid resonator and the bulk calcium fluoride resonator fabricated to confirm thermal vibration. The measured Q factor of the bulk calcium fluoride was 7.3×10^6 , and the measured Q value of the hybrid resonator was 2.2×10^7 .

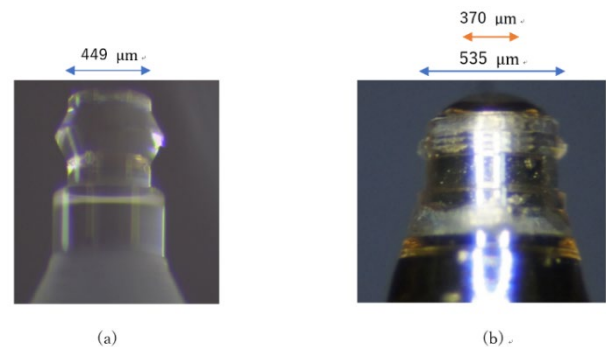


Fig. 1: Microscope image of the fabricated microcavity. (a) Normal microcavity. (b) Hybrid microcavity.

3. Measurement of TOM oscillation of calcium fluoride microresonator

Fig. 2 shows the transmission spectrum when laser light is input into the bulk calcium fluoride resonator shown in Fig. 1 (a). This is in good agreement with the TOM oscillation shown in the previous study [5]. The TOM oscillation cycle was 6.3 ms.

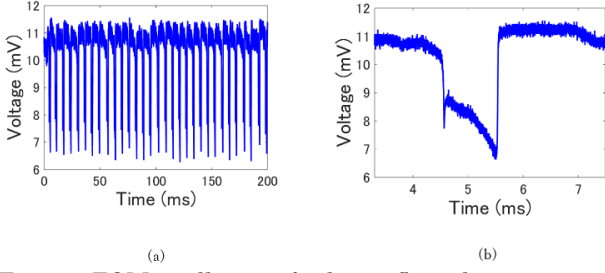


Fig. 2: TOM oscillation of calcium fluoride microcavity. (a) Over a long time period. (b) Over a short time period.

Fig. 3 shows the transmission spectrum when laser light is input into the hybrid resonator shown in Fig. 1 (b). The TOM oscillation cycle was 15 ms. Furthermore, each oscillation was composed of a small oscillation with a period of 30 μ s, as shown in Fig. 3 (b). The above results confirmed that when the calcium fluoride resonator with the hybrid structure is used, the TOM oscillation is not suppressed, but the thermal characteristic of microresonator is completely changed.

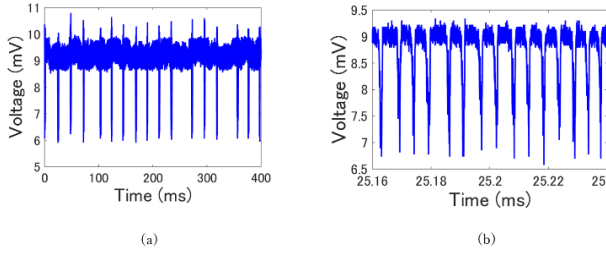


Fig. 3: TOM oscillation of hybrid microcavity. (a) Over a long time period. (b) Over a short time period.

4. Calculation of TOM oscillation of calcium fluoride microresonator

In this section, thermal vibration is considered by calculation. The resonant frequency ω_0 shifts as the effective refractive index n and the resonator length L change. This includes the thermo-optic effect and thermal expansion, and the resonant frequency shift $\delta\omega_0(t)$ taking these factors into consideration is described as follows [6].

$$\delta\omega_0(t) = -\omega_0 \left(\frac{1}{n} \frac{dn}{dT} \Delta T_1(t) + \frac{1}{L} \frac{dL}{dT} \Delta T_2(t) \right) \quad (1)$$

The right-hand side and the right-hand term of this equation represent the thermo-optic effect and thermal expansion, respectively. T is the temperature, and ΔT_1 and ΔT_2 represent the temperature change of the mode part and the entire structure, respectively. Considering the resonance frequency shift, the coupled mode equation describing the optical coupling in the microresonator and coupled waveguide is as follows.

$$\frac{da_0(t)}{dt} = -\frac{\kappa}{2} a_0(t) - i\{\omega_p - (\omega_0 + \delta\omega_0(t))\} a_0(t) + \sqrt{\kappa_c} s_{in}(t) \quad (2)$$

$a_0(t)$ is the light field inside the resonator, $s_{in}(t)$ is the input field of the waveguide, ω_p is the pump frequency, κ is the attenuation rate of the light energy inside the resonator, and κ_c is the attenuation rate of the coupled conduction caused by the output to the waveguide. ΔT_1 and ΔT_2 are determined by the temperature increase induced by the resonant light and the rate of heat diffusion in the corresponding resonator sections. The time change is expressed by the following equation.

$$\frac{d\Delta T_j(t)}{dt} = -\gamma_{th,j} \Delta T_m(t) + \gamma_{abs,j} \times P_{cav} \quad (3)$$

Here, the value of 1 or 2 enters j , which represents the temperature change related to the thermo-optic effect and the thermal expansion, respectively. $\gamma_{th,j}$ and $\gamma_{abs,j}$ are coefficients related to the speed of heat diffusion and the temperature increase caused by resonant light, and the units are Hz and K/J. Fig. 4 shows the calculation results for a typical transmittance change considering the TOM oscillation of the resonance frequency using Eqs. (1), (2) and (3). The experimental results for the TOM oscillation of a calcium fluoride microresonator shown in Section 3 agrees well with Fig. 4.

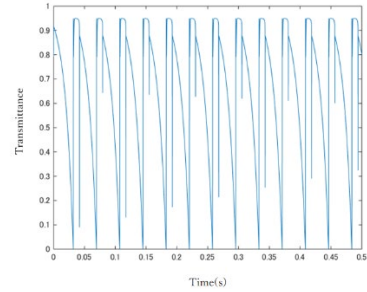


Fig. 4: TOM oscillation of calcium fluoride microcavity.

Next, we consider the way in which the TOM oscillation changes by considering the Kerr effect. In Eq. (1), the amount of resonant frequency shift $\delta\omega_0(t)$ when the Kerr effect is included is described as follows.

$$\delta\omega_0(t) = -\omega_0 \left(\frac{1}{n} \frac{dn}{dT} \Delta T_1(t) + \frac{1}{L} \frac{dL}{dT} \Delta T_2(t) + \frac{n_2}{n A_{eff}} P_{cav}(t) \right) \quad (4)$$

Here, n_2 is the nonlinear refractive index, and A_{eff} is the effective mode area. Fig. 5 shows the calculation results for the TOM oscillation when the Kerr effect is considered. It can be confirmed that large and small oscillations are generated by the Kerr effect.

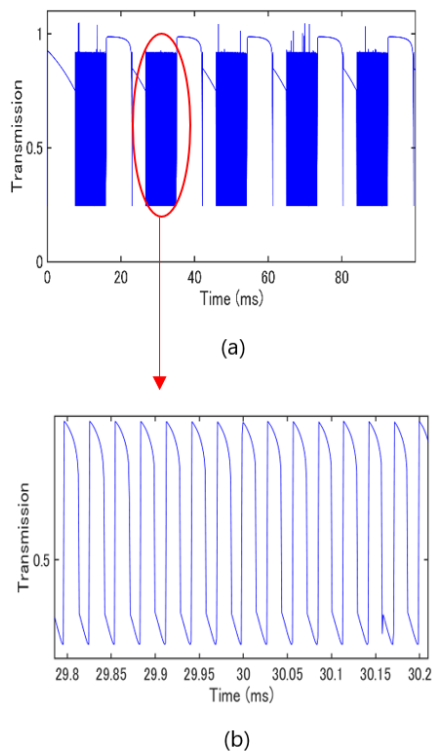


Fig. 5: TOM oscillation of calcium fluoride microcavity within the Kerr effect. (a) Over a long time period. (b) In detail.

Next, we consider the change in the TOM oscillation caused by the thermal relaxation rate $\gamma_{th,2}$. The hybrid resonator has a structure where a hole is formed at the center of the calcium fluoride microresonator and a heat sink is inserted, so that the light propagates to the resonance part and the refractive index changes due to the temperature change of that part. We can expect thermal expansion rather than the thermal effect to be suppressed. In Eq. (3), the coefficients contributing to thermal expansion are $\gamma_{th,2}$ and $\gamma_{abs,2}$. Here, we focus on the coefficient $\gamma_{th,2}$ that contributes to heat diffusion, and how the TOM oscillation of the calcium fluoride microresonator can be changed by controlling this parameter. With a calcium fluoride microresonator (diameter 500 μm), the value of the thermal relaxation rate is $\gamma_{th,2} = 3.28 \times 10^2$ (Hz). Fig. 6 shows the calculation results for TOM oscillation when $\gamma_{th,2}$ is changed. For simplicity, the Kerr effect is not considered.

Fig. 6 confirms that the TOM oscillation cycle becomes longer as $\gamma_{th,2}$ becomes larger. According to previous research, the $\gamma_{th,2}$ value of the hybrid resonator is $\gamma_{th,2} = 7.840 \times 10^2$ (Hz), which is more than twice that of a bulk calcium fluoride microresonator. In the experiment, thermal oscillation was observed in the hybrid resonator, so the $\gamma_{th,2}$ value is believed to be much smaller than this value. We consider that the calcium fluoride thickness is insufficiently reduced and the heat insufficiently diffused to the heat sink.

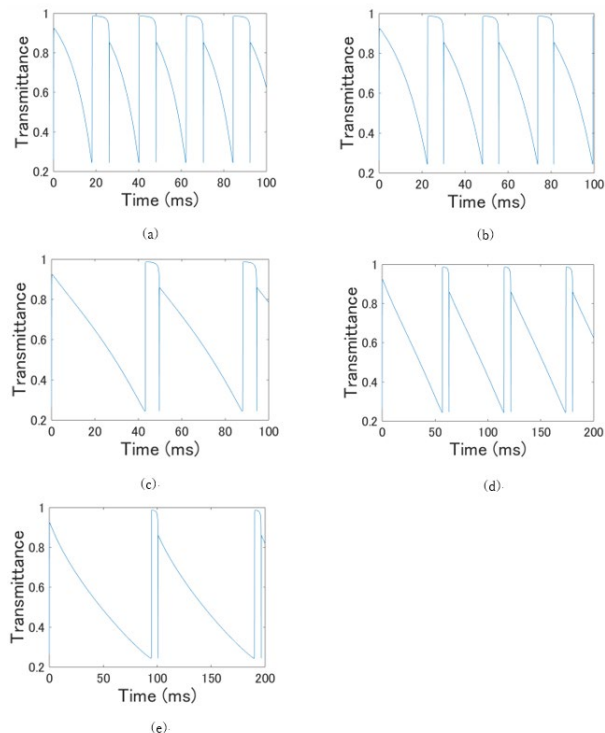


Fig. 6: TOM oscillation of calcium fluoride microcavity. (a) $\gamma_{th,2} = 3.00 \times 10^2$ (Hz). (b) $\gamma_{th,2} = 3.28 \times 10^2$ (Hz). (c) $\gamma_{th,2} = 3.75 \times 10^2$ (Hz). (d) $\gamma_{th,2} = 3.85 \times 10^2$ (Hz). (e) $\gamma_{th,2} = 3.95 \times 10^2$ (Hz).

5. Conclusion

We proposed a calcium fluoride microresonator with a hybrid structure to suppress the TOM oscillation of the calcium fluoride microresonator. However, the TOM oscillation was not suppressed and the thermal characteristics changed completely. We confirmed the reason for the thermal characteristic change by calculation.

References

- [1] W. Liang, et al., *Science* **361**, eaan8083 (2018).
- [2] T. Carmon, et al., *Opt. Express* **12**, 4742-4750 (2004).
- [3] I. S. Grudinin, et al., *Phys. Rev. A* **74**, 063806 (2006).
- [4] C. Lecaplain et al., *Nat. Commun.* **7**, 13383 (2006).
- [5] H. Itobe, et al., *AIP adv.* **6**, 055116 (2016).
- [6] Y. Deng, et al., *Opt. Lett.* **38**, 4413-4416 (2013).
- [7] H. Itobe, Master. Thesis (Keio University, 2016).

Fabrication of Er-doped Microresonator for On-chip Mode-locked Laser with CNT as Saturable Absorber

Riku Imamura(B4)

A high- Q microcavity can confine light in a small space, and thus enable a strong interaction between light and matter. A microresonator-based mode-locked laser has a high pulse repetition rate. There is the possibility of realizing a passive mode-locked laser with CNTs as a saturable absorber and an erbium-doped microresonator. In this work, we fabricate a microresonator directly from erbium doped sol-gel film deposited onto a silicon substrate and obtain single/multi-mode lasing at ~ 1580 nm for an excitation of ~ 1480 nm. We describe in detail how to fabricate the microresonator by the sol-gel method and report its optical properties.

Keyword: Microresonator, erbium-doped device, mode-locked laser

1. Background

Fiber-based mode-locked (ML) lasers provide high performance while being relatively inexpensive. The generation of high-repetition-rate pulses is gaining interest, but it remains a challenge to achieve a GHz repetition rate with fiber lasers because of their long cavity length. On the other hand, whispering-gallery-mode (WGM) microresonators allow the strong confinement of light and miniaturizing an ML laser into a WGM microresonator will enable us to achieve a high repetition rate, a small footprint and on-chip integrability. We explore the possibility of realizing a passive ML laser with the system shown in Fig. 1. There are two key technologies involved; one is saturable absorption (SA) and the other is laser gain in a microresonator. We selected a carbon nanotube (CNT) as a saturable absorber and erbium as the laser gain medium. Our group demonstrated SA in a microresonator experimentally by growing CNTs selectively on a silica microtoroid by chemical vapor deposition. By performing a pump-probe-like experiment we successfully characterized the SA behavior in a microresonator system. This is the first demonstration of SA in a WGM microcavity system [1].

We then fabricated an active erbium-doped microtoroid by using the sol-gel method. And we also obtained single-mode and multi-mode lasing with a threshold of $1.2 \mu\text{W}$ for the fabricated Er-doped microtoroid.

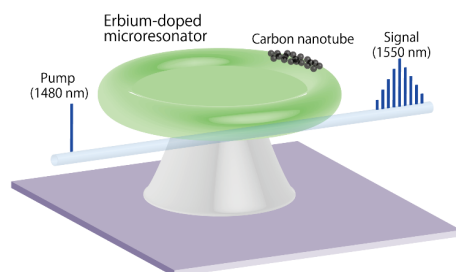


Fig. 1. Schematic illustration of a mode-locked laser with CNTs and an Er-doped microresonator.

2. Fabrication of Er-doped microresonator

Silica microtoroids are usually fabricated by processes that employ thermally grown silica film on a silicon wafer [2]. However, there is no way to dope thermally grown silica with erbium. So, we fabricated Er-doped silica film by using the sol-gel method. The sol-gel method is one way of forming silica from a metal alkoxide precursor. Although this method has been widely used, it is still a challenge to fabricate high-quality defect-free silica film on a silicon wafer that allows us to fabricate an ultrahigh- Q WGM microresonator.

The processes that can be used to fabricate an Er-doped microtoroid include forming Er-doped sol-gel silica film, photolithography, wet etching, dry etching, and laser reflow [3]. Three processes are used to fabricate a homogeneous sol-gel layer. First, sol-gel precursor solution (sol) is prepared in a snap vial by mixing tetraethyl orthosilicate (TEOS) in ethanol. Then, water (H_2O) and hydrochloric acid (HCl) (prepared at $\text{pH} \sim 2$) are mixed with sol as a catalyst. The TEOS, ethanol, H_2O weight ratio is 10:10:4.0. Er^{3+} ions are doped by adding $\text{Er}(\text{NO}_3)_3 \cdot n\text{H}_2\text{O}$. After mixing, the solution is stirred at 160 rpm for 10 min at 70°C . Second, the solution is spin-coated on a silicon wafer at 4000 rpm for 40 sec. Note that the substrate is O_2 plasma ashed to remove polymer from the silicon wafer. Third, the coated film is annealed in a tube furnace at 1000°C for 10 min to remove the solvent, and the polymeric film becomes dense thin film. As a result, we obtained sol-gel film with a thickness of ~ 300 nm. A $\sim 1.5 \mu\text{m}$ thick silica layer is needed to fabricate the microtoroid, so we repeated the formation processes to realize a stack of 6 layers. Finally, we obtained a clean film with a thickness of $\sim 1.8 \mu\text{m}$ as shown in Fig. 2(d). There are certain issues regarding the sol-gel film fabrication processes. Fig. 2(a)-(c) shows the fabricated films, Fig. 2(a) shows cracking, Fig. 2(b) shows de-wetting and Fig. 2(c) shows peeling. The cracking pattern is caused by shrinkage resulting from the evaporation of water and organic residues during annealing. De-wetting occurs when there is a low moisture content, and it results in an incomplete silica network. Peeling is caused by incomplete binding between layers. Finally, we determined the optimum parameters and obtained a clean film as shown in Fig. 2(d).

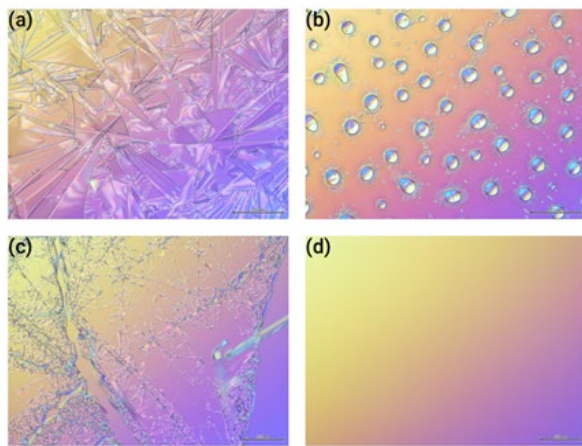


Fig. 2. Microscope images showing surfaces of sol-gel films. (a) Cracking pattern. (b) De-wetting pattern. (c) Peeling pattern. (d) Homogeneous film.

We confirmed that by carrying out photolithography, BHF etching, XeF₂ gas etching and CO₂ laser reflow with the prepared sol-gel silica film, we could produce an Er-doped silica microtoroid as with a standard silica toroid resonator. The Q -factor of an undoped toroidal resonator fabricated by the sol-gel method is 1.6×10^7 at ~ 1480 nm. This is the same Q -factor as that of a standard toroidal cavity obtained using a thermal oxidation method, and it means that it is possible to fabricate a resonator equivalent to a standard one by the sol-gel method.

Then, we calculate and estimate the erbium doping concentration. By combining the coupling mode theory and the rate equation, we can express the relationship between the erbium doping concentration and the lasing threshold. When the diameter of the resonator is $40 \mu\text{m}$, it is calculated that the doping concentration should be about $2.0 \times 10^{18} \text{ cm}^{-3}$ to realize low threshold lasing in the C-band.

3. Optical properties of Er-doped microresonator

The resonator is fabricated by adding erbium at the [calculated/estimated?] concentration. The diameter of the microtoroid is about $40 \mu\text{m}$, and the Q -factor is 9.5×10^5 at ~ 1480 nm. It is found that the Q value decreases due to absorption by erbium ions. Furthermore, it is confirmed visually that the entire resonator is doped with erbium, as up-conversion is observed such that the waveguide part emits green light at the resonant wavelength (inset in Fig. 3 (a)).

In addition to up-conversion, laser oscillation is observed as shown in Fig. 3(b), and single-mode oscillation at 1586 nm is obtained for an excitation of 1481 nm. Moreover, multi-mode oscillation at 1560 nm to 1590 nm is also observed at different resonant wavelengths. The threshold power in a single-mode oscillation is about $1.2 \mu\text{W}$ (Fig. 3(c)), which is a small value compared with that of about 10 mW for a fiber laser. Fig. 3(d) shows the estimated erbium doping concentration (blue line) and measured threshold power of a single-mode oscillation obtained in an Er-doped microtoroid (red point).

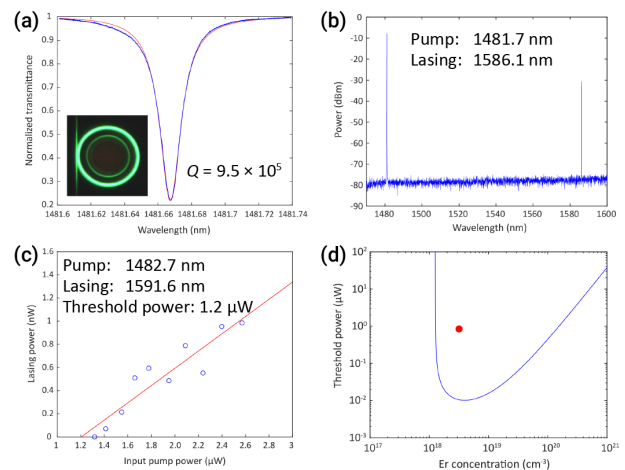


Fig. 3. (a) Measured transmission spectrum of Er-doped microtoroid fabricated by sol-gel method. The diameter is $40 \mu\text{m}$ and the doping concentration is $2.0 \times 10^{18} \text{ cm}^{-3}$. Inset is a microscope image showing up-conversion luminescence. (b) Single-mode laser spectrum at 1586 nm obtained for an excitation of 1481 nm. (c) Measured threshold power of Er-doped sol-gel silica microtoroid laser. (d) The blue line shows the estimated erbium doping concentration, and the red point is the measured threshold power of a single-mode oscillation obtained in the Er-doped microtoroid.

4. Conclusion

In this work, we establish a method for fabricating an Er-doped microtoroid by the sol-gel method for the development of an on-chip mode-locked laser. It is necessary to determine the conditions for the processes depending on the environment and the equipment used in the fabrication. The fabricated Er-doped microtoroid has a Q -factor of 9.5×10^5 at ~ 1480 nm and single/multi-mode lasing is observed around the C-band. In summary, these results represent a promising approach for realizing an on-chip high repetition rate ML WGM microresonator.

References

- [1] T. Kumagai, *et al.*, J. Appl. Phys. **123**, 233104 (2018).
- [2] D. K. Armani, *et al.*, Nature (London). **421**, 925 (2003).
- [3] L. Yang, *et al.*, J. Appl. Phys. **86**, 091114 (2005).

Theoretical analysis of mode-locking condition with Er + CNT

Mizuki Ito (B4) Ryo Suzuki (D3) Shun Fujii (D1) Takasumi Tanabe

A pulse laser requires a gain medium such as Er or Yb and a saturable absorber such as a carbon nanotube (CNT). The intracavity power can be increased by incorporating a gain medium, and a soliton can be formed by incorporating a saturable absorber. In this research, the method is applied to a silica toroid microresonator, and a theoretical study is carried out through simulation to realize a mode-locked micro-light source by combining a saturable absorber by using a CNT and gain by using Er doping.

Key words: Er, CNT, saturable absorber, NLSE, pulse laser

1. Introduction

Ti:sapphire lasers and fiber lasers are well-known types of pulse laser. A pulse laser contains a gain medium and a saturable absorber (SA) inside two reflectors, thereby generating a pulse train with a low repetition frequency ($f_{\text{rep}} \sim 0.01\text{-}10$ GHz). A pulse laser is also a mode-locked laser, and the phases of each spectrum are aligned. A saturable absorber is a substance that saturates for high-intensity incident light and acts as a transparent body; it also acts as an absorber for low-intensity incident light. Carbon nanotubes (CNT) are widely known saturable absorbers. In a ring resonator fiber laser with gain and an SA, solitons are formed using an active fiber with normal dispersion and a passive fiber with anomalous dispersion. The repetition frequency is small, and it must be increased if it is to be used for dual-comb spectroscopy and dual-comb LiDER. In this study, we aim to realize a mode-locked micro-light source that satisfies this condition. For that purpose, with a microresonator as a platform, we model an Er-doped microresonator and use a simulation to derive the amount of doped Er needed for mode-locking.

2. Theory

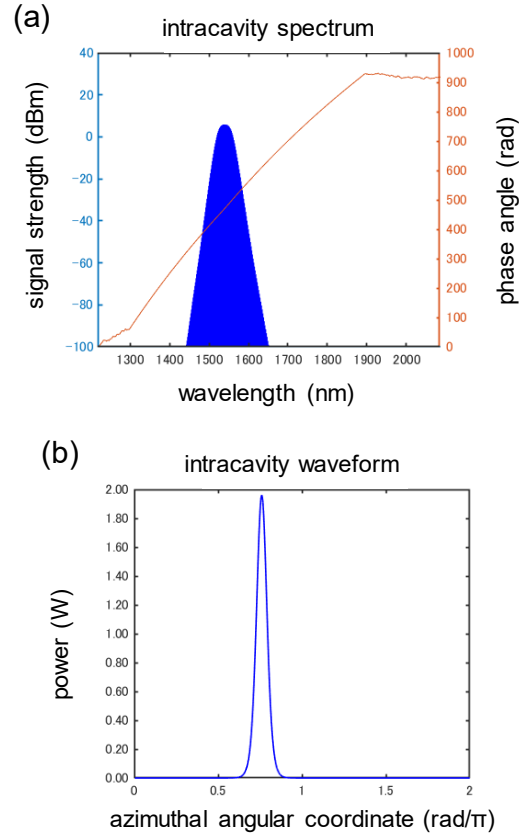
For modeling, we introduce the Er and SA gain into the nonlinear Schrödinger equation (NLSE). The model equation is given by

$$\begin{aligned} \frac{\partial A(\phi, t)}{\partial t} = & -\frac{\kappa}{2} + \frac{1}{2}(N_2 - N_1)B\hbar\omega_0 g(\nu) + i\frac{D_2}{2}\frac{\partial^2 A}{\partial \phi^2} \\ & + ig|A|^2 \\ & + \frac{1}{2}\tau_R^{-1}\log\left\{1 - \frac{q_0}{1 + \frac{|E(\phi, t)|^2}{P_A}}\right\} \end{aligned} \quad (1)$$

The loss of the microresonator, the gain realized by Er doping, the second dispersion, the Kerr effect, and the saturable absorption are shown from right to left. Also, for each coefficient, $|A|^2$ [-] is the number of photons, κ [s^{-1}] is the loss of the microresonator, D_2 [s^{-1}] is the

second-order dispersion, g [s^{-1}] is the Kerr coefficient, ϕ [rad] is the azimuth angle coordinate, t [s] is slow time, N_i [m^{-3}] is the level ion density, B [$J^{-1} \cdot m^3 \cdot s^{-1}$] is Einstein's B coefficient, ω_0 [s^{-1}] is the central angular frequency, \hbar [$J \cdot s$] is the Dirac constant, $g(\nu)$ [s^{-1}] is the shape function, and τ_R [s] is the time it takes light to travel around the microresonator. The simulation is performed by dividing equation (1) into nonlinear terms (Kerr effect and saturable absorption) and linear terms (gain loss and second-order dispersion) using the split-step Fourier method.

3. Simulation result



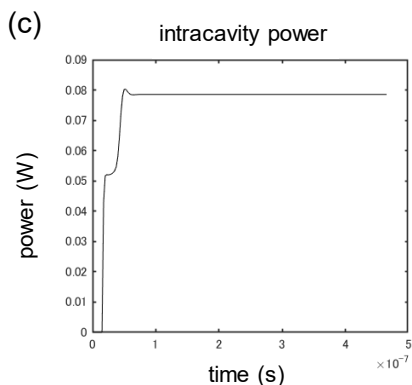


Fig. 1: (a) Intracavity spectrum. The left vertical axis represents the signal strength, and the right vertical axis represents the phase angle of each spectrum. (b) Intracavity waveform. (c) Intracavity power. (a), (b), (c) are graphs for the same time.

The phase relationship in Fig. 1 (a) is mode-locked. The reason for the curve is considered to be the influence of the variance. That is, Fig. 1 (a) shows that the pulse is formed by balancing the gain and SA, and mode-locking is achieved. Fig. 1 (b) reveals that a pulse is formed in the microresonator. Due to the effect of saturable absorption, the complex movement of the intracavity power as the spectrum rises will take on the shape of a pulse and settle as time passes. Also, due to the randomness of the initial noise, the position in the microresonator at which the pulse is formed varies from simulation to simulation. With the intracavity power in Fig. 1 (c), the power in the microresonator increases with the increase in gain and settles into a steady-state after a certain amount of time has elapsed. It can be seen that the power does not become infinite in the resonator and has a certain saturation level. The saturation power is related to the gain term, namely the population inversion, and can be obtained from the rate equation. Here, it is given by a constant. Next, we calculate the approximate amount of doped erbium. The gain term due to Er doping is represented by the following term in the NLSE [1].

$$\frac{1}{2}(N_2 - N_1)B\hbar\omega_0g(v) \quad (2)$$

Since the ratio of the upper level to the lower level in a steady state of erbium is 7:3, this is used to determine the total doping amount. In Fig. 1, we performed the calculation by setting equation (2) as $7 \times 10^{11} [\text{s}^{-1}]$ and found that the required total amount of doped Er is $3.75 \times 10^{29} [\text{m}^{-3}]$. That is $3.75 \times 10^{-23} [\text{cm}^{-3}]$. When we consider that the amount of doped Er, $2 \times 10^{19} [\text{cm}^{-3}]$, at which weak excitation occurred when a silica toroid microresonator was doped with erbium, which was reported in 2004 by L.

Yang et al., this value can also be evaluated in terms of relevance [2]. Finally, with regard to the amount of Er doping related to the gain term and the constant q_0 , which determines the SA due to the CNT related to the loss term, the behavior of the waveform in the resonator when the two variables are represented by the vertical and horizontal axes are shown as a color map.

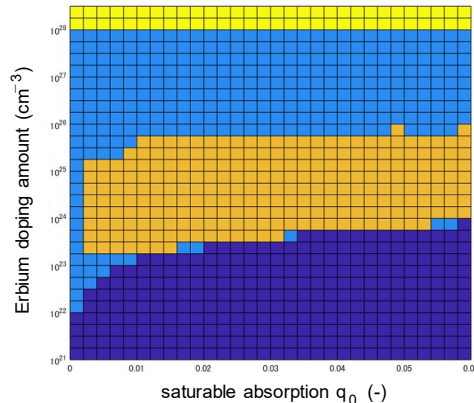


Fig. 2: Relationship between the amount of doped Er and saturable absorption in an intracavity spectrum. Deep blue indicates a state below threshold oscillation. Bright blue indicates a state of multimode oscillation. Orange indicates a mode-locked state. Yellow indicates an area that cannot be calculated.

In the calculation, the steady-state is reached when the gain and the loss induced by the SA are balanced in the microresonator. Therefore, if the amount of doped Er is shown on the vertical axis and the SA is on the horizontal axis, the mode-locking range is considered to have a certain width. This is also shown in Fig. 2. If the gain is too large, the region is an area that cannot be calculated. On the other hand, if the gain is small, the loss overcomes the gain and [it?] becomes less than the threshold oscillation. In addition, when the effect of the SA was set at zero or a value close to it, multimode oscillation occurred in a certain range.

4. Summary

Simulation results showed that mode-locking with gain and a saturable absorber (SA) is successful not only with a fiber laser but also with a microresonator platform. This result revealed the possibility of realizing a new mode-locked compact light source such as an Er-doped silica toroid microresonator with Er-doped gain and a SA based on a CNT.

References

- [1] A. Yariv, P. Yeh, Oxford University Press, 541 (2006).
- [2] B. Min, T. J. Kippenberg, L. Yang and K. J. Vahara, Physical Review A **70**, 033803 (2004).

Stabilization of Brillouin laser in coupled silica toroid microcavities

Yoshihiro Honda (M2)

Brillouin lasers in microcavity systems are currently attracting a lot of attention because they can be employed as platforms for narrower laser sources. In particular, the use of Brillouin lasers in coupled cavity systems can eliminate the complicated fabrication problems found with single cavity systems. But the operation of a Brillouin laser in a coupled cavity system is unstable. So, we demonstrate the stabilization of a Brillouin laser in coupled cavity system using the Pound-Drever-Hall (PDH) technique, which is a frequency stabilization method.

Key words: Stimulated Brillouin scattering (SBS), coupled microcavities, laser stabilization

1. Introduction

Stimulated Brillouin scattering (SBS) is a well-known nonlinear process in which two optical waves interact via an acoustic wave. The acoustic wave is generated via the electrostriction process. SBS in optical fiber, chip-based waveguides and microcavities has received a lot of attention because it can be employed for low-noise lasers, microwave synthesizers, slowing light and light storage. Whispering-gallery mode (WGM) microcavities with high Q factors and small mode volumes enable us to generate SBS with a low threshold power. In this research, it is necessary to match the free spectral range (FSR) to the Brillouin frequency shift (tens of GHz) by using mm-scale cavities or to prepare high-order transverse WGMs that separate the Brillouin frequency shift to generate SBS [1-3]. With these approaches, it is very difficult to fabricate microcavities for SBS because we need to control the size of the microcavities precisely or to fabricate microcavities that have two optical modes that separate the Brillouin frequency shift.

Here we explore coupled microcavities to enhance the SBS effect. When two cavities are placed close together their optical modes are turned into supermodes. The coupled cavities enable mode separation to be freely tuned, and this allows us to avoid the need for precise control of the cavity size. But, the instability of the Brillouin laser is a major problem with a coupled cavity system. So, we attempt to stabilize the Brillouin laser by incorporating the Pound-Drever-Hall (PDH) method, which is a frequency stabilization method. We attempt to lock the frequency of the pump laser to the resonance mode and the gap distance between two microcavities.

2. Frequency stabilization with PDH technique

The PDH technique is widely used to stabilize the frequency of a laser. The side lock method uses the transmittance of the cavity as the error signal. However, this method has a problem in that we do not know the direction of the shift from the lock point when the lock point is set at the resonance dip. Compared with the side lock method, the PDH technique enables us to lock the resonance dip because this method uses the phase information that is asymmetric to the resonance dip as the error signal.

Figure 1 (a) shows the experimental setup for the PDH technique. Before pumping the resonator, we modulated the pump laser with an electro-optic modulator (EOM) to generate sidebands. We then detected the transmitted light with a photodetector. By mixing the photodetector and local oscillator signals, we can obtain the phase information of the resonance mode. We input this obtained error signal input into the servo controller and locked the frequency of the pump laser to the resonance mode.

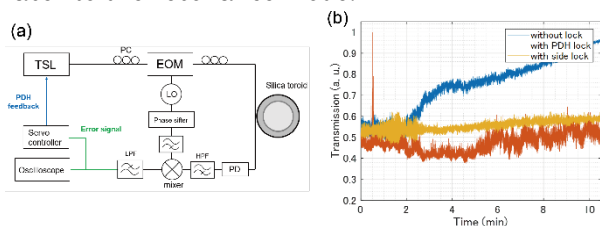


Fig. 1(a) Experimental setup for PDH locking. (b) Long-term measurement of the transmission intensity with the frequency stabilization method (side lock and PDH techniques).

In our experiment, we employed a single silica toroid microcavity to lock the pump laser to the resonance mode. The selected mode had a resonant wavelength of 1550.648 nm and a Q of 1×10^7 . The modulation frequency of the EOM was 380 MHz. Figure 1 (b) compares the way in which the transmittance of the cavity changes

temporally when the pump laser frequency is locked to the frequency of the resonant mode. This reveals that the transmittance decreased for as much as several minutes without a stabilization method, but the transmittance changed little with the PDH technique and the side lock method.

3. Stabilization for mode splitting

Next, we attempt to control the position of the two microcavities and thus stabilize mode splitting with the PDH technique. First, we measured the way in which the mode splitting fluctuated without the PDH technique as shown in Fig. 2. These results reveal that the mode splitting fluctuated 2 GHz.

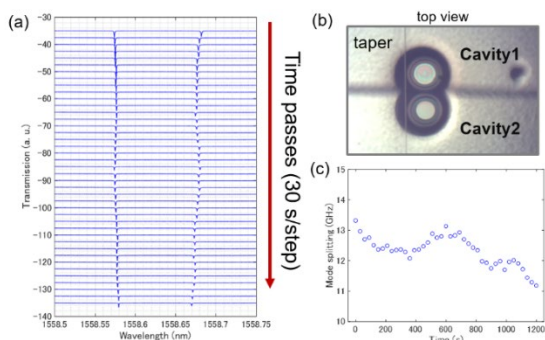


Fig. 2. (a) Transmission spectra of coupled silica toroid microcavities for different measuring times. (b) Microscope image of the coupled silica toroid microcavities. (c) Mode splitting of the supermodes for different times.

We obtained the PDH error signal in a coupled microcavity system. The experimental setup is the same as that used with the single cavity system. We measured the error signal with the oscilloscope. Figure 3 (a) shows the transmittance of the coupled microcavities (red line), and the error signal (blue line). In our experiment, the Q factor of the resonance mode was 1×10^7 , the mode splitting was 1.3 GHz, and the modulation frequency of the EOM was 380 MHz. We obtained an error signal that was in good agreement with the calculation result.

Finally, we applied the stabilization technique to the mode splitting. We set the output of the servo controller to the piezo controller in order to precisely control the position of the two microcavities. Figure 3 (b) shows the fluctuations in the mode splitting with the PDH technique. Figure 3 (c) shows the optical spectrum of the Brillouin laser output. These results reveal that we were not able to suppress the fluctuation of the mode splitting. When using piezo stages, it is important to take account of the resonant frequency of the piezo actuators. On this occasion, we did not use the high-speed piezo actuator, and the resonant frequency was only 10 Hz. In addition, the XYZ piezo stage, which incorporates

a nano-positioning system, is so heavy that the frequency range is limited. We think that this is a major cause of the failure to suppress fluctuation. As a result, although we were again able to demonstrate the Brillouin laser, we could not significantly improve the laser instability.

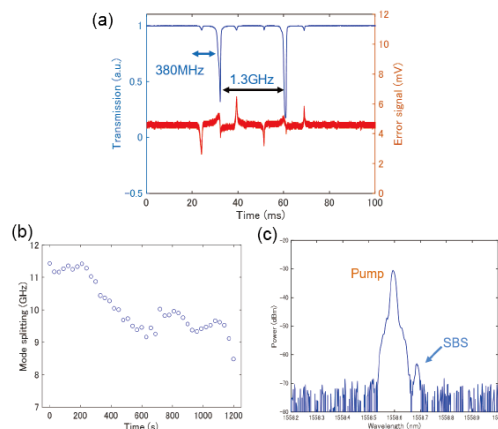


Fig. 3. (a) Experimental results for PDH error signal in coupled microcavity system. (b) Mode splitting of the supermodes for different times with the PDH technique. (c) Optical spectrum of the SBS light.

5. Conclusion

In our study, we investigated Brillouin lasers in a coupled cavity system. Here, to deal with the [Brillouin laser instability/instability of the Brillouin laser frequency?] of the coupled cavity system, we proposed and investigated an experimental setup incorporating two feedback systems. First, we demonstrated that the frequency of the pump laser was locked to the resonant frequency by using the PDH technique. Moreover, we proposed the precise position control of a coupled cavity system with the PDH technique to stabilize mode splitting. We were able to acquire the error signal in the mode splitting experimentally. The piezo stages were controlled with the PDH technique, and a mode splitting stabilization experiment was conducted, but stabilization could not be demonstrated because the signal-to-noise ratio of the error signal was small and the resonant frequency of the piezo actuator was limited. However, the PDH technique proved useful as mode splitting stabilization method in a coupled cavity system.

References

- [1] I. S. Grudinin, A. B. Matsko, and L. Maleki, *Phys. Rev. Lett.* **102**, 043902 (2009).
- [2] H. Lee, T. Chen, J. Li, K. Y. Yang, S. Jeon, O. Painter, and K. J. Vahala, *Nat. Photonics* **6**, 369–373 (2012).
- [3] G. Lin, S. Diallo, K. Saleh, R. Martinenghi, J.-C. Beugnot, T. Sylvestre, and Y. K. Chembo, *Appl. Phys. Lett.* **105**, 231103(2014).

Proposal and numerical study of non-reciprocal devices with magneto-optical effect

Naotaka Kamioka (M2)

We proposed numerically and studied TE mode optical non-reciprocal devices with a magneto-optical effect using the two-dimensional finite-difference time-domain (2D-FDTD) method. We developed a 2D-FDTD program with a magneto-optical effect expressed by an asymmetric permittivity tensor, and we confirmed numerically the non-reciprocal operation of photonic crystal waveguides with integrated magneto-optical materials. We studied the relationship between the slow light effect and the magneto-optical effect. The achieved operations are expected to be applied to integrated optical isolators.

Key words : Photonic crystal; Slow light effect; Magneto-optical effect; Optical isolation

1. Introduction

Optical devices, which are becoming more widely used, need optical isolators to prevent the operation destabilizing during cascade connection [1]. Many optical isolators employ magneto-optical (MO) effects. For example, isolation has been achieved by attenuating only back-reflected light with non-reciprocal loss (NRL) [2] or destructive interference with a non-reciprocal phase shift (NRPS) [3]. However, the NRL is large and requires both strong magnetic fields and low temperatures. The NRPS can be used only for TM modes and requires an interferometer and horizontal magnetic fields.

In this work, we proposed numerically and studied photonic crystal waveguides (PCW) with integrated MO materials as seen in Fig. 1. We proposed this structure based on reports concerning the relationship between circular polarization at the side of a waveguide and propagating lights [2][4]. By generating the real and imaginary parts of the off-diagonal element of the complex permittivity tensor (ϵ'_{xy} , ϵ''_{xy}), non-reciprocal operation will be achieved (Fig. 1(a, b)). In addition, we can expect to realize enhanced operation via strong confinement or a slow light effect and develop design flexibility with the PCW structure.

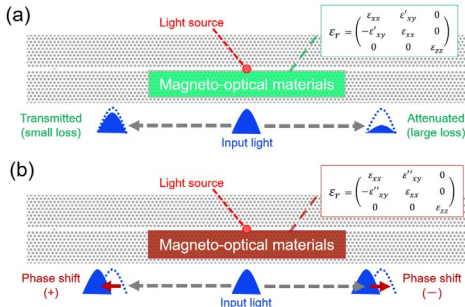


Fig. 1: Proposed structure and expected non-reciprocal operation. (a) NRL. (b) NRPS.

2. Modified FDTD method

The finite-difference time-domain (FDTD) method is a calculation method that solves temporally and

spatially discretized Maxwell equations. This is a relatively precise time-domain simulation, and so we used the FDTD method. However, the conventional FDTD method cannot deal with an asymmetric permittivity tensor, so we modified the position of the electromagnetic fields and the main equations of the FDTD method (in Fig. 2). (a) shows the spatial position of the TE modes with the conventional FDTD method, and this position setting enables us to discretize Maxwell equations. (b) shows the modified positions and this modification allows us to solve the equations with an asymmetric permittivity tensor, and we obtained the recursive formula of E_x (Eq. (1)). We achieved similar formulas for E_y, H_z and we developed a modified FDTD program. We called this method T-FDTD. In this program, we introduced the real part of the permittivity tensor as permittivity ($\epsilon_{xy} = \epsilon'_{xy}$) and the imaginary part (ϵ''_{xy}) as conductivity (σ_{xy}) by conversion.

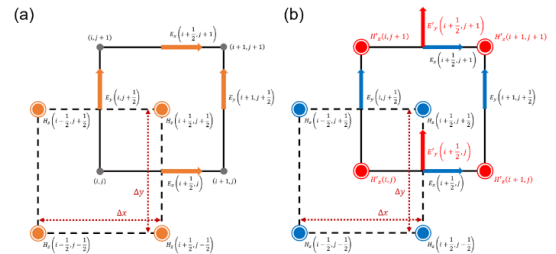


Fig. 2: (a) Conventional and (b) modified spatial position of electromagnetic fields in the FDTD method.

Fig. 3 shows an evaluation of the calculated results obtained with T-FDTD. (a)(b) are comparisons of the MEEP (conventional FDTD, blue graph) and T-FDTD (modified FDTD, red graph) transmission spectra when (a) $\epsilon'_{xy} = \epsilon'_{yx} = 0$ and (b) $\epsilon'_{xy} = \epsilon'_{yx} = 0.4$. We confirmed that the transmissions were simulated well with both settings. (c) shows that the propagation time error was less than one time step Δt (quantization error) and the reflection rate error at the boundary was below 1.5 %, thus the T-FDTD method was quantitatively evaluated and found to be sufficiently precise.

$$E_x^n \left(i + \frac{1}{2}, j \right) = \frac{P_{yx}^- P_{xy}^+ - P_{yy}^+ P_{yx}^-}{P_{xx}^+ P_{yy}^+ - P_{yx}^+ P_{xy}^+} E_x^{n-1} \left(i + \frac{1}{2}, j \right) + \frac{P_{yy}^- P_{xy}^+ - P_{xy}^- P_{yy}^+}{P_{xx}^+ P_{yy}^+ - P_{yx}^+ P_{xy}^+} E_y^{n-1} \left(i + \frac{1}{2}, j \right) + \frac{1}{P_{xx}^+ P_{yy}^+ - P_{yx}^+ P_{xy}^+} \times \left\{ 2\Delta t P_{yy}^+ / \Delta y \left(H_z^{n-\frac{1}{2}} \left(i + \frac{1}{2}, j + \frac{1}{2} \right) - H_z^{n-\frac{1}{2}} \left(i + \frac{1}{2}, j - \frac{1}{2} \right) \right) + 2\Delta t P_{xy}^+ / \Delta x \left(H_z^{n-\frac{1}{2}} \left(i + 1, j \right) - H_z^{n-\frac{1}{2}} \left(i, j \right) \right) \right\} \quad \left(p_{ij}^\pm = \sigma_{ij} \Delta t \pm 2\varepsilon_{ij} \right) \quad (1)$$

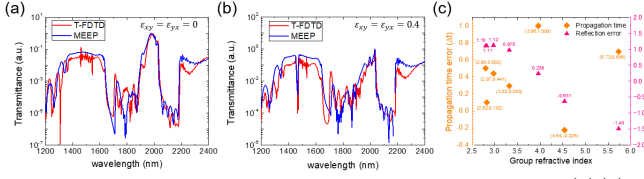


Fig. 3: Evaluations of developed FDTD method. (a)(b) Comparisons of calculated transmission spectra obtained using MEEP and T-FDTD with (a) $\varepsilon'_{xy} = \varepsilon'_{yx} = 0$ or (b) $\varepsilon'_{xy} = \varepsilon'_{yx} = 0.4$. (c) Propagation time (orange) and reflection rate (pink) errors induced by changing the permittivity tensor.

3. NRL simulation results

Fig. 4 shows the simulated NRL results. (a) is the proposed structure and we used graphene as the MO material and parameters taken from previous research [5]. (b) and (c) are the monitored intensities of H_z with or without (b) $\varepsilon'_{xy} = -\varepsilon'_{yx} = 0.143$ (corresponds to 1.3 T external magnetic fields) and (c) $\varepsilon'_{xy} = -\varepsilon'_{yx} = 0.929$ (corresponds to 8.4 T). From the ratios of these intensities, the achieved isolation ratios (IRs) are 1.31 dB/19.2 μm and 6.56 dB/19.2 μm , respectively.

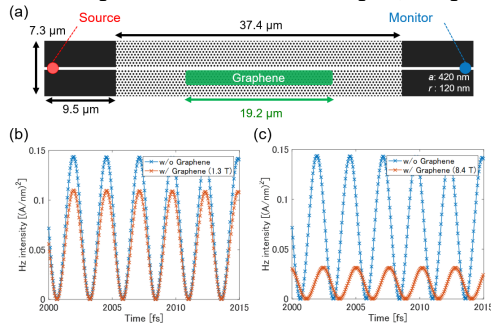


Fig. 4: Calculated NRL with the parameters of graphene. (a) Structure and settings. (b)(c) Observed intensities of magnetic fields H_z at the monitor with an external magnetic field of (b) 1.3 T or (c) 8.4 T.

Fig. 5 shows numerical studies of NRL. (a) and (b) are graphs of monitored magnetic fields H_z vs. (a) time or (b) IR with different ε'_{xy} values. (c) and (d) are the graphs of H_z vs. (c) time or (d) IR with different lengths of MO materials. (e) shows the spectrum of the isolation ratio and the group refractive index of PCW. From these results, we achieved the expected isolation operation and enhancement of IR caused by the slow light effect of the PCW.

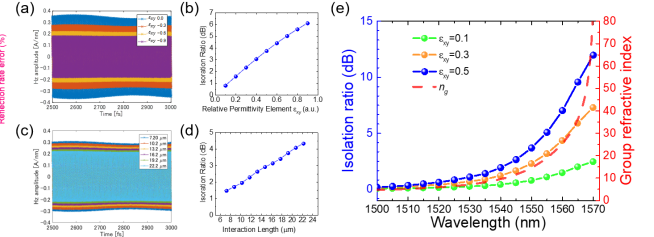


Fig. 5: Numerical studies of NRL. (a)(b) H_z and IR vs. ε'_{xy} . (c)(d) H_z and IR vs. material length. (e) IR spectrum with group refractive index.

4. NRPS simulation results

Fig. 6 shows the calculated NRPS results. (a) shows the structure. We assumed Ce:YIG as the MO material and used the parameters from [6]. (b) shows the monitored intensities of H_z with or without $\varepsilon''_{xy} = -\varepsilon''_{yx} = -0.0073$ (equivalent to $\sigma_{xy} = -0.0785$ S/m and corresponding to an external magnetic field of about 1 T). We achieved a phase shift (PS) of $1.83 \times 10^{-2} \pi$ / 170.5 μm .

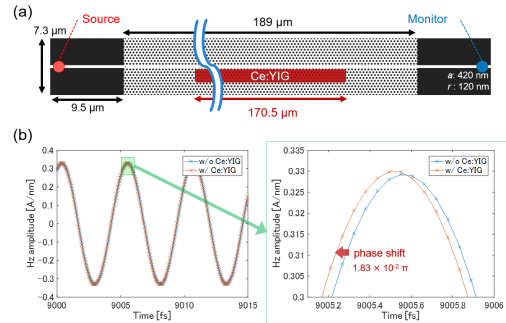


Fig. 6: Calculated NRPS with Ce:YIG parameters. (a) Structure and settings. (b) Observed H_z with or without external magnetic fields.

Fig. 7 shows numerical studies of NRPS. (a) and (b) are the graphs of monitored magnetic fields H_z vs. (a) time or (b) PS with different σ_{xy} values. (c) and (d) are graphs of H_z vs. (c) time or (d) PS with different lengths of MO materials. (e) shows the spectrum of the PS and the group refractive index of PCW. Although we achieved the expected NRPS and some proportional connections, the direct enhancement of the PS by the slow light effect was not achieved.

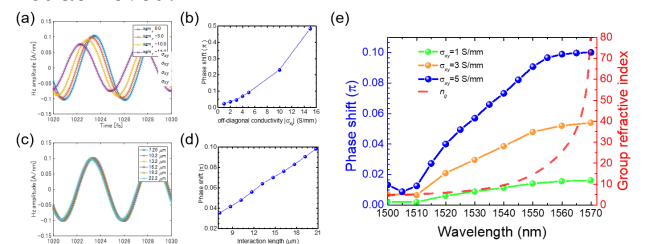


Fig.7: Numerical studies of NRPS. (a)(b) H_z and PS vs. ε'_{xy} . (c)(d) H_z and PS vs. material length. (e) PS spectrum with the group refractive index.

In conclusion, we studied and confirmed the possibility of realizing the proposed non-reciprocal devices and slow light enhancement by PCW.

References

- [1] P. David, Y. Zongfu, and F. Shanhui, Nat. Photonics **3**, 116 (2009).
- [2] J. Ma, *et al.*, Appl. Phys. Lett. **108**, 151103(2016).
- [3] Y. Shoji and T. Mizumoto, Sci. Tech. Adv. Mater. **15.1**, 014602 (2014).
- [4] J. Petersen *et al.*, Science, **346**, 67(2014).
- [5] H. Dötsch, *et al.*, J. Opt. Soc. Am. B **22(1)**, 240 (2005).
- [6] M. C. Onbasli, *et al.*, Sci. Rep. **6**, 23640 (2016).

Statistical Data

Publications (Apr. 2018 – Mar. 2019)

Journal papers

- [1] Y. Mizumoto, H. Itobe, H. Kangawa, M. Fuchida, T. Tanabe, and Y. Kakinuma, “Development of CaF₂-brass hybrid WGM microcavity by using ultra-precision machining,” *Mechanical Engineering Letters*, Vol. 4, pp. 17-00491 (8 pages) (2018).
- [2] R. Suzuki, A. Kubota, A. Hori, S. Fujii, and T. Tanabe, “Broadband gain induced Raman comb formation in a silica microresonator,” *J. Opt. Soc. Amer. B*, Vol. 35, No. 4, pp. 933-938 (2018). (Editor’s pick) [arXiv:1712.05091v1]
- [3] Y. Honda, W. Yoshiki, T. Tetsumoto, S. Fujii, K. Furusawa, N. Sekine, and T. Tanabe, “Brillouin lasing in coupled silica toroid microcavities,” *Appl. Phys. Lett.*, Vol. 112, 201105 (5 pages) (2018). (Featured Article) (Scilight) [arXiv:1712.09000v1]
- [4] T. Kumagai, N. Hirota, K. Sato, K. Namiki, H. Maki, and T. Tanabe, “Saturable absorption by carbon nanotubes on silica microtoroids,” *J. Appl. Phys.*, Vol. 123, 233104 (6 pages) (2018).
- [5] S. Fujii, Y. Okabe, R. Suzuki, T. Kato, A. Hori, Y. Honda, and T. Tanabe, “Analysis of mode coupling assisted Kerr comb generation in normal dispersion system,” *IEEE Phot. J.*, Vol. 10, No. 5, 4501511 (11 pages) (2018).
- [6] N. A. B. Daud and T. Tanabe, “Photolithographically fabricated silicon photonic crystal nanocavity photoreceiver with laterally integrated p-i-n diode,” *AIP Adv.*, Vol. 8, No. 10, 105224 (7 pages) (2018).
- [7] R. Suzuki, S. Fujii, A. Hori, and T. Tanabe, “Theoretical study on dual-comb generation and soliton trapping in a single microresonator with orthogonally polarized dual-pumping,” *IEEE Phot. J.*, Vol. 11, No. 1, 6100511 (11 pages) (2019).

International conferences

- [1] S. Fujii, M. Hasegawa, R. Suzuki, T. Tanabe, “Nonlinear Parametric Oscillation Phase-matched via High-order Dispersion in High-Q Silica Toroid Microresonators,” *The 7th Advances Lasers and Photon Sources Conference (ALPS’18)*, ALPS5-II-7, Yokohama, April 24-27 (2018).
- [2] R. Suzuki, A. Kubota, A. Hori, S. Fujii, and T. Tanabe, “Raman comb generation through broadband gain in a silica microresonator,” *CLEO:2018, SW3A.7*, San Jose, May 13-18 (2018).
- [3] T. Tanabe, R. Suzuki, Y. Honda, and S. Fujii “Frequency comb and Brillouin lasing in optical microcavities,” *Asia Pacific Laser Symposium (APLS)*, F1, Xi’an, May 28-31 (2018). (invited)
- [4] T. Tanabe “Brillouin lasing in a coupled toroid microcavities system,” *CLEO Pacific Rim 2018*, WS7-5, HongKong, Jul 29-Aug 3 (2018). (invited)
- [5] S. Fujii, R. Suzuki, M. Hasegawa, and T. Tanabe, “Kerr comb generation under weak dispersion regime in high-Q silica microtoroids,” *CLEO Pacific Rim 2018*, Tu3H.4, HongKong, Jul 29-Aug

- 3 (2018).
- [6] R. Suzuki, S. Fujii, A. Hori, and T. Tanabe, “Soliton trapping in a Kerr microresonator with orthogonally polarized dual-pumping,” CLEO Pacific Rim 2018, W1B.3, HongKong, Jul 29-Aug 3 (2018).
 - [7] R. Ishida and T. Tanabe, “Strong MoS₂ photoluminescence on graphen for coupling with silica microcavity,” CLEO Pacific Rim 2018, W3A.4, HongKong, Jul 29-Aug 3 (2018).
 - [8] S. Jin, Y. Ooka, T. Tetsumoto, N. A. Daud, N. Kamioka, T. Okamura, and T. Tanabe, “Improved CMOS compatible photonic crystal demultiplexer,” CLEO Pacific Rim 2018, W4H.3, HongKong, Jul 29-Aug 3 (2018).
 - [9] N. A. Daud, T. Tetsumoto, and T. Tanabe, “Photolithographically Fabricated Silicon Photonic Crystal Nanocavity Photoreceiver with a Laterally Integrated Pin Diode,” Progress In Electromagnetics Research Symposium (PIERS), 2P15a-3, Toyama, Aug 1-4 (2018). 2,160 kB
 - [10] T. Tanabe, S. Fujii, R. Suzuki, and Y. Honda, “Microcavity based laser sources: Microresonator frequency comb and Brillouin lasing,” 23rd Microoptics Conference (MOC2018), H1, Taipei, Oct 15-18 (2018). (invited)
 - [11] T. Tanabe, R. Suzuki, and S. Fujii, “Kerr comb generation in a mode coupled system,” SPIE Photonics West, 10904-20, San Francisco, Feb 2-7 (2019). (invited)
 - [12] T. Tanabe, “Brillouin Laser in Coupled Microresonator System,” The 3rd Workshop on OptoMechanics and Brillouin Scattering (WOMBAT2019), We8.1, Tel-Aviv, Mar 26-18 (2019). (invited)

Awards

Shun Fujii, “The 7th Advanced Lasers and Photon Sources, Best Student Award” (Apr 2018)

Publications (Apr. 2018 – Mar. 2019)

Journal papers

- [1] Y. Mizumoto, H. Itobe, H. Kangawa, M. Fuchida, T. Tanabe, and Y. Kakinuma, “Development of CaF₂-brass hybrid WGM microcavity by using ultra-precision machining,” *Mechanical Engineering Letters*, Vol. 4, pp. 17-00491 (8 pages) (2018).
- [2] R. Suzuki, A. Kubota, A. Hori, S. Fujii, and T. Tanabe, “Broadband gain induced Raman comb formation in a silica microresonator,” *J. Opt. Soc. Amer. B*, Vol. 35, No. 4, pp. 933-938 (2018). (Editor’s pick) [arXiv:1712.05091v1]
- [3] Y. Honda, W. Yoshiki, T. Tetsumoto, S. Fujii, K. Furusawa, N. Sekine, and T. Tanabe, “Brillouin lasing in coupled silica toroid microcavities,” *Appl. Phys. Lett.*, Vol. 112, 201105 (5 pages) (2018). (Featured Article) (Scilight) [arXiv:1712.09000v1]
- [4] T. Kumagai, N. Hirota, K. Sato, K. Namiki, H. Maki, and T. Tanabe, “Saturable absorption by carbon nanotubes on silica microtoroids,” *J. Appl. Phys.*, Vol. 123, 233104 (6 pages) (2018).
- [5] S. Fujii, Y. Okabe, R. Suzuki, T. Kato, A. Hori, Y. Honda, and T. Tanabe, “Analysis of mode coupling assisted Kerr comb generation in normal dispersion system,” *IEEE Phot. J.*, Vol. 10, No. 5, 4501511 (11 pages) (2018).
- [6] N. A. B. Daud and T. Tanabe, “Photolithographically fabricated silicon photonic crystal nanocavity photoreceiver with laterally integrated p-i-n diode,” *AIP Adv.*, Vol. 8, No. 10, 105224 (7 pages) (2018).
- [7] R. Suzuki, S. Fujii, A. Hori, and T. Tanabe, “Theoretical study on dual-comb generation and soliton trapping in a single microresonator with orthogonally polarized dual-pumping,” *IEEE Phot. J.*, Vol. 11, No. 1, 6100511 (11 pages) (2019).

International conferences

- [1] S. Fujii, M. Hasegawa, R. Suzuki, T. Tanabe, “Nonlinear Parametric Oscillation Phase-matched via High-order Dispersion in High-Q Silica Toroid Microresonators,” *The 7th Advances Lasers and Photon Sources Conference (ALPS’18)*, ALPS5-II-7, Yokohama, April 24-27 (2018).
- [2] R. Suzuki, A. Kubota, A. Hori, S. Fujii, and T. Tanabe, “Raman comb generation through broadband gain in a silica microresonator,” *CLEO:2018, SW3A.7*, San Jose, May 13-18 (2018).
- [3] T. Tanabe, R. Suzuki, Y. Honda, and S. Fujii “Frequency comb and Brillouin lasing in optical microcavities,” *Asia Pacific Laser Symposium (APLS)*, F1, Xi’an, May 28-31 (2018). (invited)
- [4] T. Tanabe “Brillouin lasing in a coupled toroid microcavities system,” *CLEO Pacific Rim 2018, WS7-5*, HongKong, Jul 29-Aug 3 (2018). (invited)
- [5] S. Fujii, R. Suzuki, M. Hasegawa, and T. Tanabe, “Kerr comb generation under weak dispersion regime in high-Q silica microtoroids,” *CLEO Pacific Rim 2018, Tu3H.4*, HongKong, Jul 29-Aug

- 3 (2018).
- [6] R. Suzuki, S. Fujii, A. Hori, and T. Tanabe, “Soliton trapping in a Kerr microresonator with orthogonally polarized dual-pumping,” CLEO Pacific Rim 2018, W1B.3, HongKong, Jul 29-Aug 3 (2018).
- [7] R. Ishida and T. Tanabe, “Strong MoS₂ photoluminescence on graphen for coupling with silica microcavity,” CLEO Pacific Rim 2018, W3A.4, HongKong, Jul 29-Aug 3 (2018).
- [8] S. Jin, Y. Ooka, T. Tetsumoto, N. A. Daud, N. Kamioka, T. Okamura, and T. Tanabe, “Improved CMOS compatible photonic crystal demultiplexer,” CLEO Pacific Rim 2018, W4H.3, HongKong, Jul 29-Aug 3 (2018).
- [9] N. A. Daud, T. Tetsumoto, and T. Tanabe, “Photolithographically Fabricated Silicon Photonic Crystal Nanocavity Photoreceiver with a Laterally Integrated Pin Diode,” Progress In Electromagnetics Research Symposium (PIERS), 2P15a-3, Toyama, Aug 1-4 (2018). 2,160 kB
- [10] T. Tanabe, S. Fujii, R. Suzuki, and Y. Honda, “Microcavity based laser sources: Microresonator frequency comb and Brillouin lasing,” 23rd Microoptics Conference (MOC2018), H1, Taipei, Oct 15-18 (2018). (invited)
- [11] T. Tanabe, R. Suzuki, and S. Fujii, “Kerr comb generation in a mode coupled system,” SPIE Photonics West, 10904-20, San Francisco, Feb 2-7 (2019). (invited)
- [12] T. Tanabe, “Brillouin Laser in Coupled Microresonator System,” The 3rd Workshop on OptoMechanics and Brillouin Scattering (WOMBAT2019), We8.1, Tel-Aviv, Mar 26-18 (2019). (invited)

Awards

Shun Fujii, “The 7th Advanced Lasers and Photon Sources, Best Student Award” (Apr 2018)

Dissertations

PhD thesis:

Nurul Ashikin Binti Daud, “Photolithographically fabricated photonic crystal nanocavity as modulator and receiver,”
Feb. 2019. Ryo Suzuki, “Investigation into the effects of optical nonlinearities on microresonator frequency combs,”
Feb. 2019.

Master thesis:

Naotaka Kamioka, “Proposal and numerical study on non-reciprocal devices with magneto-optical effect”
Akihiro Kubota, “Fabrication of high-Q crystalline magnesium fluoride optical microresonators and experiments
for dissipative Kerr soliton generation”
Mika Fuchida, “Fabrication of high-Q magnesium fluoride optical microresonator and study on
dissipative Kerr Soliton generation”
Yoshihiro Honda, “Stabilization for Brillouin laser in coupled silica toroid microcavities”

Bachelor thesis:

Mizuki Ito, “Modelling of Er-doped microresonator by nonlinear Schrödinger equation for theoretical analysis.
Riku Imamura, “Fabrication of Er-doped Microresonator for On-chip Mode-locked Laser with CNT as Saturable
Absorber”
Shuya Tanaka, “Precise Dispersion Measurement of Ultra-high Q Microresonator for soliton generation”
Koichiro Handa, “Thermal vibration control using calcium fluoride crystal microresonator”

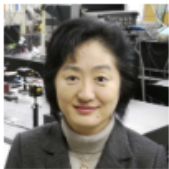
Symposium



KEIO Symposium on
Microresonator Frequency Comb

December 4 (Tue.) - 6 (Thu.), 2018
Keio University, Hiyoshi Campus, Yokohama, Japan

Keynote speakers



Kaoru Minoshima (The University of Electro-Communication, Japan)

"Optical Frequency Comb Applications beyond Frequency Metrology by use of Versatile Optical Wave Manipulation"



Kerry J. Vahala (Caltech, USA)

"Soliton Microcombs for Miniature Spectrometers, Optical Synthesizers, and Clocks"



Andrew M. Weiner (Purdue University, USA)

"Generation and Manipulation of High Rate Optical Frequency Combs: Classical and Quantum"

Invited speakers



Yanne K. Chembo (FEMTO-ST, France)

"Nonlinear photonics using ultra-high Q whispering-gallery mode resonators"



Tobias Hansson (Linköping University, Sweden)

"Dynamics of Frequency Combs in Cubic and Quadratic Microresonators"



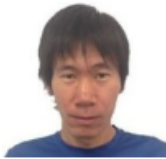
Tobias Herr (Swiss Center for Electronics and Microtechnology, Switzerland)

"Frequency combs in synchronously-driven microresonators"



Atsushi Ishizawa (NTT Basic Research Laboratories, Japan)

"Electro-optics-modulation (EOM) combs"



Naoya Kuse (IMRA America, Inc., USA)

"Optical frequency comb with 10^{-18} frequency instability"



Junqiu Liu (EPFL, Switzerland)

"Ultralow-Power Photonic Chip-Based Soliton Microcombs"



Pablo Marin-Palomo (KIT, Germany)

"Coherent Optical Communications with Microresonator-Based Frequency Combs"



Andrey Matsko (OEwaves, USA)

"Integrated Kerr Frequency Comb RF Photonic Oscillators"



Tomoyuki Miyaji (Meiji University, Japan)

"Mathematical Understanding of Kerr Frequency Combs From a Viewpoint of A Pattern-Formation Phenomenon"



Norihiko Nishizawa (Nagoya University, Japan)

"Wideband, wavelength tunable optical frequency comb generation at NIR and MIR region based on fiber lasers"



Yoshitomo Okawachi (Columbia University, USA)

"On-Chip Frequency Combs"



Scott B. Papp (National Institute of Standards and Technology, USA)

"Design/use frequency combs with Kerr-optics and electro-optics"



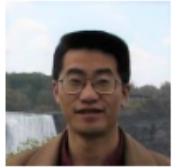
Hiroyuki Sasada (Keio University, Japan)

"Precise mid-infrared molecular spectroscopy using an optical frequency comb"



Sze Yun Set (The University of Tokyo, Japan)

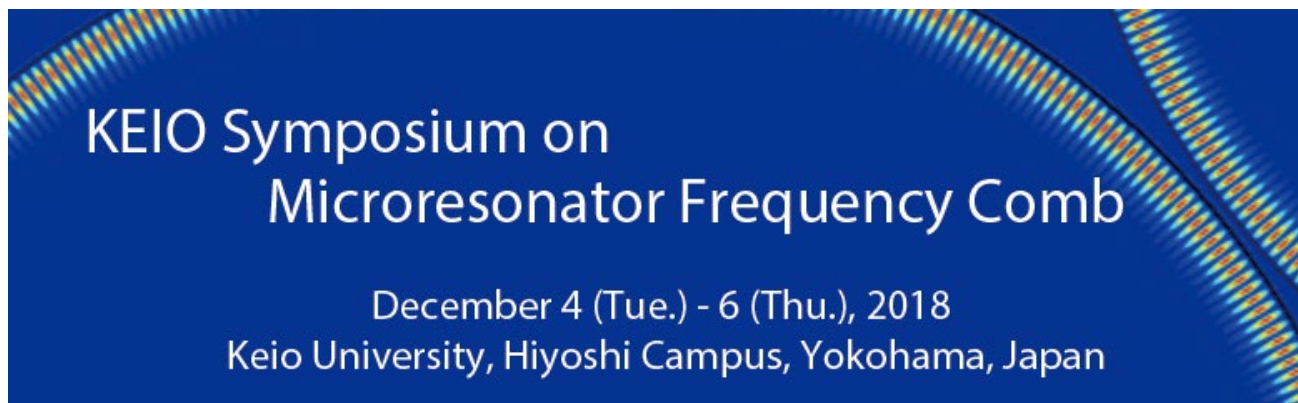
"Ultrafast fiber lasers for frequency comb generation"



Changzheng Sun (Tsinghua University, China)

"Broadband Optical Frequency Comb Generation in Epitaxially Grown AlN Microresonators"

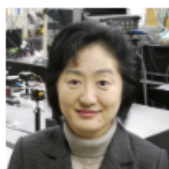
Symposium



**KEIO Symposium on
Microresonator Frequency Comb**

December 4 (Tue.) - 6 (Thu.), 2018
Keio University, Hiyoshi Campus, Yokohama, Japan

Keynote speakers



Kaoru Minoshima (The University of Electro-Communication, Japan)

"Optical Frequency Comb Applications beyond Frequency Metrology by use of Versatile Optical Wave Manipulation"



Kerry J. Vahala (Caltech, USA)

"Soliton Microcombs for Miniature Spectrometers, Optical Synthesizers, and Clocks"



Andrew M. Weiner (Purdue University, USA)

"Generation and Manipulation of High Rate Optical Frequency Combs: Classical and Quantum"

Invited speakers



Yanne K. Chembo (FEMTO-ST, France)

"Nonlinear photonics using ultra-high Q whispering-gallery mode resonators"



Tobias Hansson (Linköping University, Sweden)

"Dynamics of Frequency Combs in Cubic and Quadratic Microresonators"



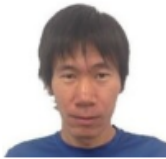
Tobias Herr (Swiss Center for Electronics and Microtechnology, Switzerland)

"Frequency combs in synchronously-driven microresonators"



Atsushi Ishizawa (NTT Basic Research Laboratories, Japan)

"Electro-optics-modulation (EOM) combs"



Naoya Kuse (IMRA America, Inc., USA)

"Optical frequency comb with 10^{-18} frequency instability"



Junqiu Liu (EPFL, Switzerland)

"Ultralow-Power Photonic Chip-Based Soliton Microcombs"



Pablo Marin-Palomo (KIT, Germany)

"Coherent Optical Communications with Microresonator-Based Frequency Combs"



Andrey Matsko (OEwaves, USA)

"Integrated Kerr Frequency Comb RF Photonic Oscillators"



Tomoyuki Miyaji (Meiji University, Japan)

"Mathematical Understanding of Kerr Frequency Combs From a Viewpoint of A Pattern-Formation Phenomenon"



Norihiko Nishizawa (Nagoya University, Japan)

"Wideband, wavelength tunable optical frequency comb generation at NIR and MIR region based on fiber lasers"



Yoshitomo Okawachi (Columbia University, USA)

"On-Chip Frequency Combs"



Scott B. Papp (National Institute of Standards and Technology, USA)

"Design/use frequency combs with Kerr-optics and electro-optics"



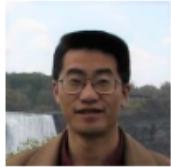
Hiroyuki Sasada (Keio University, Japan)

"Precise mid-infrared molecular spectroscopy using an optical frequency comb"



Sze Yun Set (The University of Tokyo, Japan)

"Ultrafast fiber lasers for frequency comb generation"



Changzheng Sun (Tsinghua University, China)

"Broadband Optical Frequency Comb Generation in Epitaxially Grown AlN Microresonators"